

The OTELO survey

Faint end of the luminosity function of [O II]3727 emitters at $\langle z \rangle = 1.43$

Bernabé Cedrés^{1,2}, Ángel Bongiovanni^{3,4}, Miguel Cerviño⁵, Jakub Nadolny^{1,2}, Jordi Cepa^{1,2,4}, José A. de Diego^{6,1}, Ana María Pérez García^{5,4}, Jesús Gallego⁷, Maritza A. Lara-López⁸, Miguel Sánchez-Portal^{3,4}, J. Ignacio González-Serrano^{9,4}, Emilio J. Alfaro¹⁰, Rocío Navarro Martínez⁴, Ricardo Pérez Martínez^{11,4}, J. Jesús González¹², Carmen P. Padilla Torres^{1,2,13}, Héctor O. Castañeda^{14,†}, and Mauro González^{1,2}

¹ Instituto de Astrofísica de Canarias (IAC), 38200 La Laguna, Tenerife, Spain
e-mail: bcedres@iac.es

² Departamento de Astrofísica, Universidad de La Laguna (ULL), 38205 La Laguna, Tenerife, Spain

³ Instituto de Radioastronomía Milimétrica (IRAM), Av. Divina Pastora 7, Núcleo Central 18012, Granada, Spain

⁴ Asociación Astrofísica para la Promoción de la Investigación, Instrumentación y su Desarrollo, ASPID, 38205 La Laguna, Tenerife, Spain

⁵ Centro de Astrobiología (CSIC/INTA), 28692 ESAC Campus, Villanueva de la Cañada, Madrid, Spain

⁶ Instituto de Astronomía, Universidad Nacional Autónoma de México, Apdo. Postal 70-264, 04510 Ciudad de México, Mexico

⁷ Departamento de Física de la Tierra y Astrofísica, Instituto de Física de Partículas y del Cosmos, IPARCOS. Universidad Complutense de Madrid, E-28040, Madrid, Spain

⁸ DARK, Niels Bohr Institute, University of Copenhagen, Lyngbyvej 2, Copenhagen DK-2100, Denmark

⁹ Instituto de Física de Cantabria (CSIC-Universidad de Cantabria), E-39005 Santander, Spain

¹⁰ Instituto de Astrofísica de Andalucía, CSIC, E-18080, Granada, Spain

¹¹ ISDEFE for European Space Astronomy Centre (ESAC)/ESA, P.O. Box 78, E-28690, Villanueva de la Cañada, Madrid, Spain

¹² Instituto de Astronomía, Universidad Nacional Autónoma de México, 04510 Ciudad de México, Mexico

¹³ Fundación Galileo Galilei, Telescopio Nazionale Galileo, Rambla José Ana Fernández Pérez, 7, 38712 Breña Baja, Tenerife, Spain

¹⁴ Departamento de Física, Escuela Superior de Física y Matemáticas, Instituto Politécnico Nacional, 07738 Ciudad de México, Mexico

ABSTRACT

Aims. In this paper, we aim to study the main properties and luminosity function (LF) of the [O II]3727 emitters detected in the OTELO survey in order to characterise the star formation processes in low-mass galaxies at $z \sim 1.43$ and to constrain the faint-end of the LF.

Methods. Here, we describe the selection method and analysis of the emitters obtained from narrow-band scanning techniques. In addition, we present several relevant properties of the emitters and discuss the selection biases and uncertainties in the determination of the LF and the star formation rate density (SFRD).

Results. We confirmed a total of 60 sources from a preliminary list of 332 candidates as [O II]3727 emitters. Approximately 93% of the emitters have masses in the range of $10^8 < M_*/M_\odot < 10^9$. All of our emitters are classified as late-type galaxies, with a lower value of $(u - v)$ when compared with the rest of the emitters of the OTELO survey. We find that the cosmic variance strongly affects the normalisation (ϕ^*) of the LF and explains the discrepancy of our results when compared with those obtained from surveys of much larger volumes. However, we are able to determine the faint-end slope of the LF, namely, $\alpha = -1.42 \pm 0.06$, by sampling the LF down to ~ 1 dex lower than in previous works. We present our calculation of the SFRD of our sample and compare it to the value obtained in previous studies from the literature.

Key words. techniques: imaging spectroscopy – surveys – catalogs – galaxies: starburst – galaxies: luminosity function, mass function – galaxies: star formation – cosmology: observations

1. Introduction

The luminosity function (LF) is a powerful tool used in characterising the distribution of star-forming galaxies at cosmological scales. By observing different emission lines, it is possible to trace the star-formation activity at different redshifts and, thus, at different epochs of the evolution of galaxies. Taking into account that the strongest emission line in a star-forming galaxy is usually H α , this line can be considered the first probe for LFs (see e.g. Lilly et al. 1995, where their redshift sample ranges at $0 < z < 1.3$; Geach et al. 2008 at $z = 2.23$; Sobral et al. 2013 at

$0.40 < z < 2.23$; Sobral et al. 2015 at $z = 0.8$; Khostovan et al. 2020 at $z = 0.47$; Ly et al. 2007 at $0.08 < z < 0.40$; or more recently, Hayashi et al. 2020 at $0.09 < z < 0.48$; and Harish et al. 2020 at $z \sim 0.62$).

Other lines may be used when looking for other windows of observation in redshift, where H α is not available. For example, the next most luminous line of the Balmer series, H β was employed for determining the LF at $z \sim 0.9$ by Navarro Martínez et al. (2020). Other works have used the combination of H β and [O III], for example De Barros et al. (2019) reaching as far as $z \sim 8$; Khostovan et al. (2015) up to $0.84 <$

$z < 3.24$; and Sobral et al. (2015) up to $z = 1.4$. In addition, there are a series of works where the LF is obtained by employing the doublet [O II] $\lambda\lambda 4959, 5007$ alone, for example, in Ly et al. (2007) at $0.41 < z < 0.84$; Bongiovanni et al. (2020) at $z \sim 0.83$; Khostovan et al. (2020) at $0.91 < z < 1.10$; or Hayashi et al. (2020) at $0.05 < z < 0.94$.

In order to sample the LF at very high redshift regimes, the Lyman α emitters are the objects of choice. For example, Ouchi et al. (2008), Sobral et al. (2018), and Herenz et al. (2019) obtained LFs at $3.1 < z < 5.7$, $2 < z < 6$, and $3 < z < 6$, respectively.

Going back to intermediate redshift regimes, the [O II] $\lambda\lambda 3726, 29$ doublet, it is also a good candidate for the study of the LF. It is located in the bluest part of the spectrum in rest frame, when compared with H α , [O III] $\lambda\lambda 4959, 5007$, and H β , allowing us to reach larger values of the redshift from ground observations and avoiding the less transparent parts of the atmosphere in the infrared regime. The LF has been derived for this doublet by a number of authors who have employed spectroscopy or narrow-band techniques (Gallego et al. 2002 for the local universe; Khostovan et al. 2015 for $1.47 < z < 4.69$; Khostovan et al. 2020 for $1.57 < z < 1.9$; Drake et al. 2013 for $0.35 < z < 1.64$; Ly et al. 2007 for $0.89 < z < 1.47$; Comparat et al. 2015 for $0.1 < z < 1.65$; or Hayashi et al. 2020 for $0.41 < z < 1.60$). It has also been simulated from $z = 0.1$ to $z = 3.0$ by Park et al. (2015).

Nevertheless, at $z > 1$, the faint end of the [O II] $\lambda\lambda 3727$ LF has not been properly observed. Indeed, almost all studies have not been capable of going beyond a $\log(L[\text{O II}]3727) \simeq 41$ [erg s $^{-1}$] in the best of cases (see e.g. the discussion in Khostovan et al. 2015). We believe that it is paramount to reach as low as possible in terms of luminosity in order to study the evolution of low-mass galaxies. For example, according to Sobral et al. (2011), the environment may be responsible for the slope of the faint end of the LF, being steeper for low-density regions and shallower for high-density fields. Moreover, the correct determination of the slope of the faint end of the LF influences the integration of the LF itself and, therefore, may vary the determination of the cosmic star formation history (SFH).

In this work, we take advantage of the sources detected in the OTELO survey (see Bongiovanni et al. 2019) to generate a catalogue of [O II] $\lambda\lambda 3727$ emitters at $z \sim 1.43$. We study the physical properties of these sources and we extend the study of the faint end of the LF for the [O II] $\lambda\lambda 3727$ line to constrain the faint end slope and. In addition, we obtain the star formation rate density (SFRD) at this redshift.

The paper is organised as follows. In Section 2, we describe the OTELO survey and the selection of the sources. In Section 3, we present several of the derived properties from the data, including the extinction, the line fluxes, the morphology, and the stellar masses. In Section 4, we discuss the derived equivalent width of the emitters, in addition to studying a handful of high equivalent-width galaxies and comparing our results with those from the literature. Section 5 is devoted to our derived LF and the SFRD, along with a comparison with similar data from the literature. In Section 6, we summarise our main conclusions. For all the calculations carried out in this work, we assumed a standard Λ CDM cosmology with $\Omega_\Lambda = 0.7$, $\Omega_m = 0.3$, and $h_0 = 0.7$.

2. The OTELO survey data and selection of the sources

2.1. The OTELO survey

In this work, we take advantage of the OTELO survey catalogue and its data products (for an in-depth description, see Bongiovanni et al. 2019). As a summary, the OTELO survey is a 2D spectroscopic blind survey covering a region of 56 arcmin 2 of the Extended Groth Field. It has a resolution of $R \sim 700$, covering a 230 Å of a selected atmospheric window (around 8950-9300 Å) that is relatively free of sky emission lines. The catalogue contains a total of 11237 sources and it is 50% complete at an AB magnitude of 26.38. From these sources, 5322 preliminary emission line candidates were selected according to the following criteria: (i) at least one point of the pseudo-spectrum lies above a value defined by $f_c + 2 \times \sigma_c$, where f_c is the flux of the pseudo-continuum, defined as the median flux of the pseudo-spectra, and σ_c is the root of the averaged square deviation from f_c of the entire pseudo-spectrum; and (ii) there is an adjacent point with a flux density above $f_c + \sigma_c$ (Bongiovanni et al. 2020).

The catalogue also presents complementary reprocessed data from several other surveys. This ancillary data covers from X-ray to far-infrared (FIR), both photometric and spectroscopic. Photometric redshifts (known as z_{best}) were determined through the LePhare code (Ilbert et al. 2006), using libraries for normal and starburst galaxies, QSOs, Seyferts and stars, and fitted to the OTELO photometric data. The z_{best} is designated as the $z_{\text{BEST_deepY}}$ from Bongiovanni et al. (2019)¹

2.2. Selection of the sources

Taking into account that the [O II] $\lambda\lambda 3727, 29$ doublet must lie comfortably within the OTELO observing window of 8950-9300 Å, we selected, from the preliminary emission line candidates list, all the sources in the range of $1.40 < z_{\text{best}} < 1.50$. Using this criteria, we selected a first subset of 332 emitters.

Following the work carried out by Bongiovanni et al. (2020) for the [O III] $\lambda\lambda 4959, 5007$ emitters, and in order to produce a robust list of candidates, this first selection was visually screened by at least three researchers, looking for misidentifications, artifacts, and any other anomalies, such as truncated lines, overlapping sources, or multiple unlikely emission lines structures which appear in low signal-to-noise pseudo-spectra. From these cases, only those sources with truncated line in pseudo-spectra are considered true-positive emitters, despite their having been excluded from the final sample. However, this effect is included as a part of the sample completeness estimation described in Section 5.1. The resulting list was composed of 60 candidates. Table 1 summarises the classification determined for each one of the 332 candidates.

Employing the online tool developed for the OTELO database², at least three researchers selected a new z_{guess} by visual inspection that is closer to the real value of the redshift than the z_{best} . This z_{guess} was employed as an input for the deconvolution program. To obtain the line fluxes from the pseudo-spectra, we employed the so-called inverse deconvolution, introduced in Cedrés et al. (2013) and developed in detail in Nadolny et al. (2020). Briefly, a series of simulations (on the order of 10^6) are performed and then a χ^2 minimisation method is used to ob-

¹ It means, the best galaxy/starburst solution including the OTELO survey data as an additional photometric point.

² <http://research.iac.es/proyecto/otelo/pages/otelo.php>

	Number of objects	Percentage
Total candidates	332	100%
Selected [O II]3727 sources	60	18%
Rejection reason		
Multiple structures in low S/N pseudo-spectra	136	41%
Overlapping sources	62	18.7%
Truncated lines	55	16.6%
Misidentifications and other causes	19	5.7%

Table 1: Classification summary of emission line candidates.

tain the probability density function of the possible solutions for each source, taking the mode of the distribution as the best solution and the confidence intervals around the mode of all the associated parameters: fluxes, equivalent widths, redshifts, and continuum fluxes. In this paper, we quoted the uncertainties as the interval covering the 68% of such confidence interval. After all the candidates were deconvolved, a new visual inspection was carried out, this time to check the goodness of the fitted models. A catalogue with flux, equivalent width, redshift, and continuum flux was then generated. Following the deconvolution, z_{OTELO} is derived from the OTELO pseudo-spectra for each emitter. This new redshift is a refinement of z_{guess} .

Considering that we may have little contamination by AGNs due to our selection criteria in redshift (we only took galaxies fitted by a starburst or star-forming galaxies template), we decided not to correct for AGN contamination. Moreover, Drake et al. (2013) infer a contamination fraction about six percent in a sample of emitters at $z = 1.6$ and they suggest that AGN activity is usually associated with star-forming processes, so removing AGNs would lead to an over-correction.

We ran LePhare code a second time, but with redshift fixed to z_{OTELO} and restricted to star-forming galaxies templates with the aims of obtain a more accurate value of reddening. The applied galaxy templates are Kinney et al. (1996) and Bruzual & Charlot (2003) – with a continuous star formation law.

One example of a deconvolved pseudo-spectrum is shown in Fig. 1. Even if the source is noisy, the fitted model is good enough to extract the required information. On the other hand, in Fig. 2, we represent the pseudo-spectrum and deconvolving lines for an object with a much better signal-to-noise ratio (emitter id: 8532). In Fig.A.1 in the appendix, we represent the pseudo-spectra of all selected emitters in the catalogue.

3. Derived properties

3.1. Extinction correction

The obtained fluxes were corrected via internal extinction following the law presented in Calzetti et al. (2000) and employing the reddening $E(B - V)$ obtained as an output from the second fitting of the emitters using the LePhare code (see Bongiovanni et al. 2019). We also took into account the inherent extinction of the templates in Kinney et al. (1996) when deriving our value for the extinction.

In Fig. 3, we have represent the histogram of the derived value of $A_{[\text{O II}]3727}$ for all the emitters. The mean result is $\langle A_{[\text{O II}]3727} \rangle = 0.88 \text{ mag}$, which is equivalent to $\langle A_{H\alpha} \rangle = 0.5 \text{ mag}$,

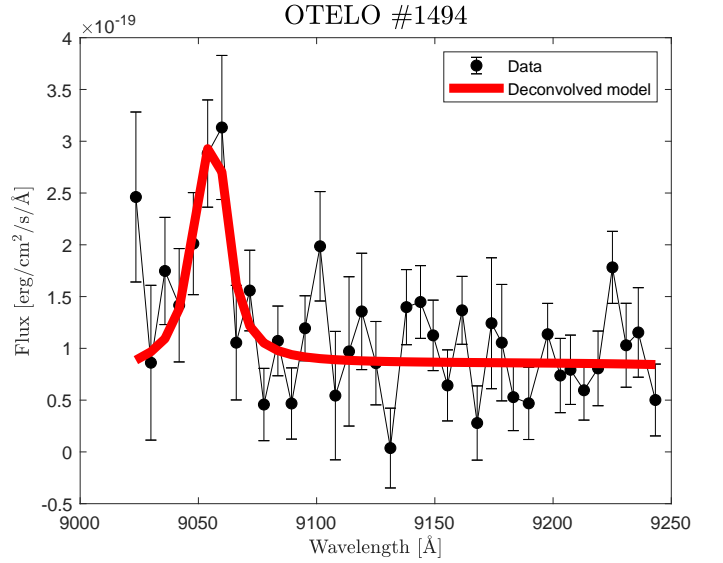


Fig. 1: Pseudo-spectra and deconvolved spectra for the id: 1494 emitter. We note the noisy aspect of the pseudo-spectra. However, in these circumstances, the model is capable of obtaining a good measure of the [O II]3727 lines.

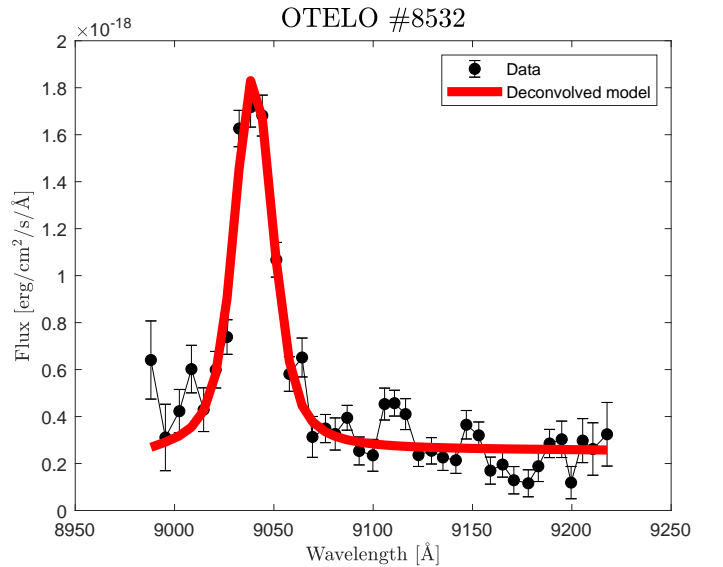


Fig. 2: Pseudo-spectra and deconvolved spectra for the id: 8532 emitter. The signal-to-noise ratio is better than in Fig. 1

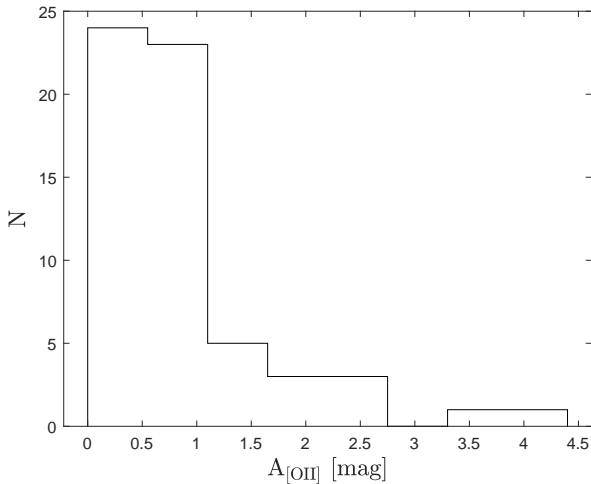


Fig. 3: Histogram of the value of $A_{[\text{OII}]3727}$ for all the emitters in the catalogue.

with a standard deviation of $\sigma = 0.5$. This is lower than the normally employed $A_{\text{H}\alpha} \sim 1$ mag. This value has been experimentally obtained, for example, by Ibar et al. (2013), who reported an $A_{\text{H}\alpha} = 1.0 \pm 0.2$ mag for objects at $z = 1.47$, employing a combination of far-IR and $\text{H}\alpha$ data. On the other hand, our result seems to agree with the trend observed in other works and cited in Hayashi et al. (2013), where the authors found that $[\text{OII}]3727$ emitters selected by narrow-band (NB) techniques are likely to be dust-poor systems. For example, both Hayashi et al. (2013) and Khostovan et al. (2020) give $A_{\text{H}\alpha} \sim 0.35$ mag for emitters at $z \sim 1.47$, Hayashi et al. (2015) found $A_{\text{H}\alpha} = 0.63$ mag for $z = 1.5$, and Khostovan et al. (2015) obtains $A_{\text{H}\alpha} = 0.55 \pm 0.12$ mag for emitters at $z = 1.59$. Nevertheless, the large dispersion of the mean value derived makes difficult to obtain a clear conclusion about the absorption nature of our emitters. As Garn et al. (2010) have pointed out, the individual extinctions vary significantly between galaxies, which is clearly visible in the histogram of Fig. 3.

3.2. Line fluxes

In Fig. 4, we represent the histogram of the measured flux for all the emitters, corrected for extinction. The lowest flux is $\log(f_{[\text{OII}]3727 \text{ min}}) = -17.72$ [erg/cm²/s], the maximum is $\log(f_{[\text{OII}]3727 \text{ max}}) = -15.56$ [erg/cm²/s], and the mean value is $\langle \log(f_{[\text{OII}]3727}) \rangle = -17.02$ [erg/cm²/s]. We can observe that only the 15% of the emitters have a flux higher than $\log(f_{[\text{OII}]3727}) = -16.75$ [erg/cm²/s].

3.3. Morphology

Following Kauffmann et al. (2003), we define the concentration index C as the ratio of the radius enclosing the 90 percent of the luminosity in a defined band over the radius enclosing the 50 percent of the luminosity in the same band. In our case, we employed the high-resolution images from the bands F814W(I) and the F606W(V) from HST/ACS. However, only 45 emitters from our sample had data in those filters. The median value for the I filter is $C_I = 1.92$. However, as shown, for example, in Strateva et al. (2001) and in Nadolny et al. (2021), this param-

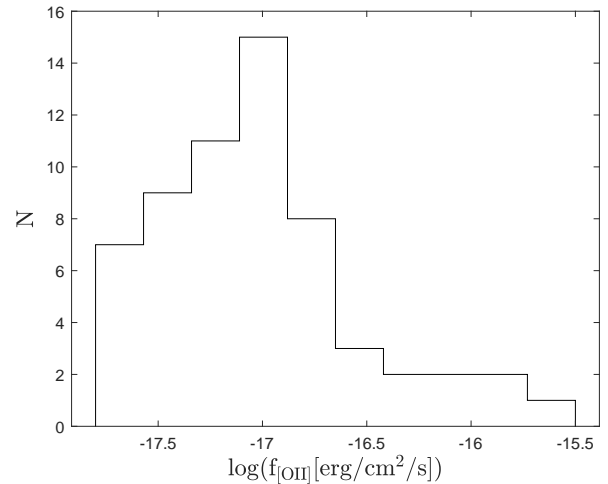


Fig. 4: Histogram of the line flux (extinction corrected) observed for all the selected emitters.

eter may only serve to establish a crude classification between early-type (ET) and late-type (LT) galaxies.

In Nadolny et al. (2021) the intensity spatial distribution of the emitters from the OTELO survey is fitted using a parametric form in a Sérsic (1968) profile, defined as:

$$I(r) = I_e \exp\{-b_n[(r/r_e)^{1/n} - 1]\}, \quad (1)$$

where r_e is the effective radius (i.e. radius containing 50% of total flux), I_e is the intensity at r_e in the filter selected (F814W or F606W from HST/ACS in this case), n is the Sérsic index, and b_n is a function of n as defined in Ciotti (1991). For a detailed description of the fitting process, see Nadolny et al. (2021). The obtained Sérsic index n is an useful tool in order to classify the morphology of the emitting sources. For disc-dominated LT galaxies, the expected value of this parameter in the I filter is $n_I < 4$ (Nadolny et al. 2021). The median values obtained for the $[\text{OII}]3727$ emitters is $n_I = 2.1 \pm 1.7$. This value appears to be slightly larger than the mean value obtained for all the emitters with enough data for the OTELO survey Nadolny et al. (2021) ($n_I = 1.3$). However most of the emitters show n_I values below the threshold for LT galaxies. On the other hand, our results are well within the range obtained by Paulino-Afonso et al. (2017), who give $n_I = 1.16^{+1.62}_{-0.72}$ for the emitters at $z = 1.47$ from High-Z Emission Line Survey (HiZELS).

We also derived the ratio of Sérsic indices in both bands $N_V^I = n_I/n_V$ (introduced by Vika et al. (2015)). This parameter is sensitive to the internal structure of the galaxy when paired with a colour term. In this case, the median value obtained was $N_V^I = 1.3 \pm 0.7$, which is well inside the error margin for the whole OTELO database, where the value was $N_V^I = 1.1 \pm 0.4$ for the LT galaxies (Nadolny et al. 2021). In Fig. 5, we reproduce the results from Nadolny et al. (2021).

The red dashed line marks the linear discriminant analysis developed by de Diego et al. (2020), employing deep learning methods for morphology classification. In the figure we can see that all the selected emitters (indicated by red circles) are comfortably distributed in the late-type locus. Moreover, almost all detected emitters are somewhat bluer than the mean of the all OTELO ET galaxies.

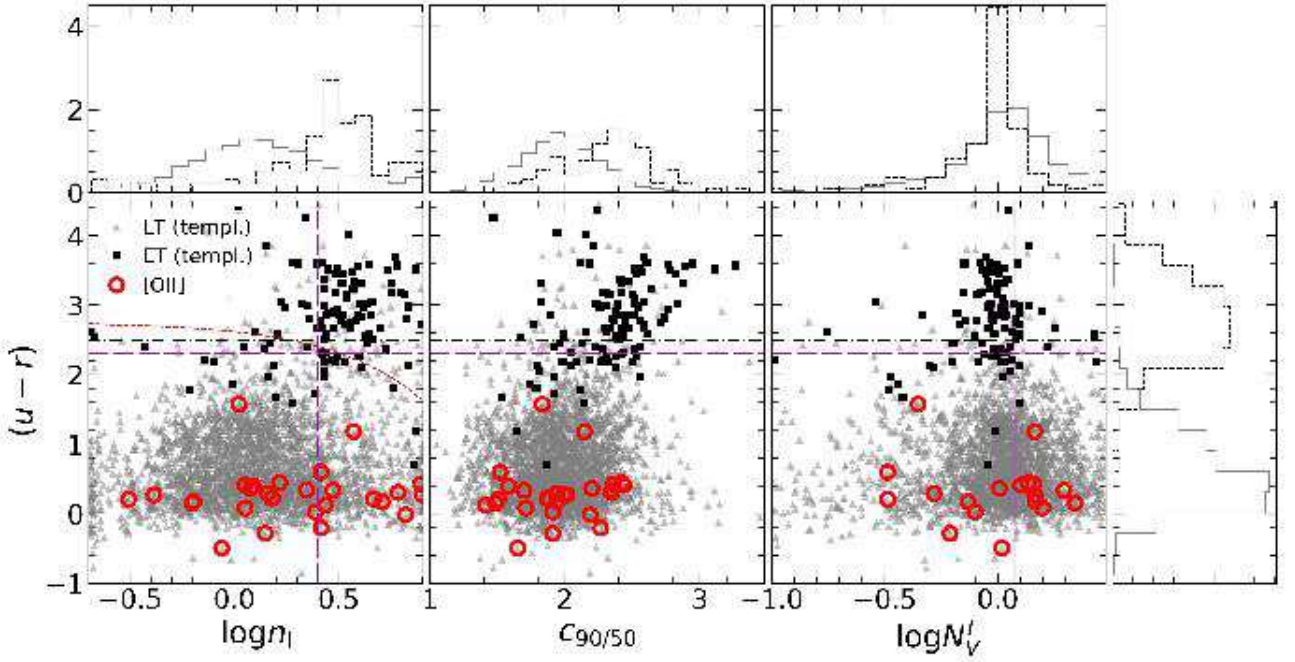


Fig. 5: Observed $(u - r)$ colour versus morphological parameters for all the sources of OTELO. From left to right: Logarithm of the Sérsic index in the filter F814W (I), concentration index for the I filter too, and the logarithm of the wavelength-dependent ratio of the Sérsic indices for I and V (F606W). Triangles and solid lines in grey (histograms) represent LT, squares and dashed lines in black (histograms) represent ET galaxies. Red circles represent the $[\text{O II}]\lambda 3727$ emitters from our sample with HST/ACS ancillary data. Top histograms corresponds to the respective value, as indicated in x-axis label, while right-hand histogram show $(u - r)$ distribution. All histograms represents density distributions. Horizontal dot-dashed line in black shows $(u - r) = 2.5$. Red dashed line shows the results from de Diego et al. (2020). Dashed lines in magenta represent limits from Vika et al. (2015): horizontal cut in $(u - r) = 2.3$, while vertical dashed-lines in magenta represent $\log(n_1) = 0.4$ and $\log(N'_V) = 0.08$. Figure adapted from Nadolny et al. (2021).

3.4. Derived masses

Following López-Sanjuan et al. (2012) we obtained an estimation of the stellar mass for 48 of the emitters in the catalogue (for a detailed description of the process, see Bongiovanni et al. 2020). The remaining 12 emitters with no stellar mass determination presented a large error in several of the ancillary bands that made it impossible to derive a meaningful value for the mass.

The median value derived for the stellar mass was $\log(M_*/M_\odot) = 8.87$, with a dispersion of $\log(M_*/M_\odot) = 0.67$. The largest mass derived was $\log(M_*/M_\odot) = 10.93$, meanwhile, the lowest mass was $\log(M_*/M_\odot) = 7.89$. If we define the low-mass population as the galaxies with $M_* < 10^{10} M_\odot$ (Bongiovanni et al. 2020), only three emitters present are out of the low-mass regime. This means that about 93% of the emitters belong to the low-mass criterion. In Bongiovanni et al. (2020), the percentage of low-mass galaxies reached 87% in a catalogue composed by 171 emitters at a $\langle z \rangle = 0.83$; meanwhile for Nadolny et al. (2020), the whole sample of $\text{H}\alpha$ emitters was in the low-mass regime, with a 63% being very low-mass galaxies ($M_* < 10^9 M_\odot$). These two results seems compatible with the stellar masses derived in our sample, indicating that the OTELO survey favours the detection of low-mass galaxies. This is a direct consequence of an ultra-deep pencil-beam designed survey, as the OTELO survey is, in fact (Bongiovanni et al. 2019). The mass distribution for the emitters is represented in Fig. 6.

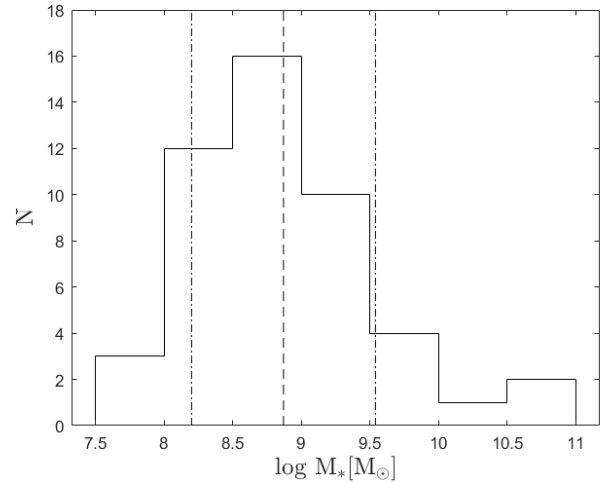


Fig. 6: Histogram of the derived stellar mass (in solar masses) for the emitters. The dashed line marks the position of the median value at $\log(M_*/M_\odot) = 8.87$ and the point-dashed lines mark $\pm 1\sigma$ over the median value.

4. $[\text{O II}]\lambda 3727$ Equivalent width

One of the parameters derived from the deconvolution is the equivalent width of the $[\text{O II}]\lambda 3727$ doublet. In Fig. 7, we represent the histogram of the logarithm of $EW_{[\text{O II}]\lambda 3727}$. The minimum value obtained in our emitters is $10 \pm 5 \text{ \AA}$ and the maximum is $185 \pm 16 \text{ \AA}$. The median value is $EW_{[\text{O II}]\lambda 3727} = 65 \text{ \AA}$, with a 1σ

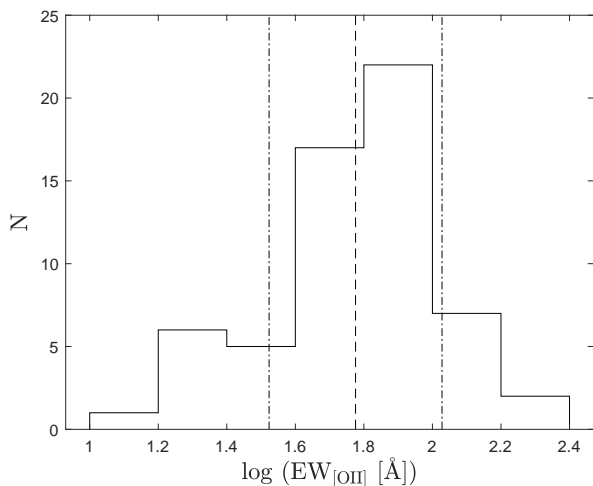


Fig. 7: Histogram of the line equivalent width for all the selected [O II]3727 emitters in OTELO. The dashed line marks the position of the median value, and the point dashed lines mark $\pm 1\sigma$ over the median value.

dispersion of $EW_{[\text{O II}]3727} = 37 \text{ \AA}$. Following Ramón-Pérez et al. (2019), in $EW_{\text{H}\alpha}$, the minimum value for detection with a probability $p \leq 0.95$ was $\sim 10.5 \text{ \AA}$. In order to estimate our detection limit, we have to translate our limit in $EW_{\text{H}\alpha}$ into a limit in $EW_{[\text{O II}]3727}$. For this reason, we can employ the relationship given by Kennicutt (1992), which is summarised in Eq. 2:

$$EW_{[\text{O II}]3727} = 0.4 \times EW_{(\text{H}\alpha + [\text{N II}])}. \quad (2)$$

However, this relationship was obtained for nearby galaxies and it also presents a large dispersion for galaxies with very strong emission lines. Nevertheless, employing Lamareille et al. (2006) data, we were able to calculate this relationship for galaxies with $0.2 < z < 1.0$. In this case, the resultant slope was 0.5 ± 0.1 , very similar to the 0.4 value from Kennicutt (1992) relationship. Based on this premise, the minimum value we would be able to detect with $p \leq 0.95$ is $\sim 4.2 \text{ \AA}$. In this case, it is clear that all our emitters are well over this threshold.

In Huang et al. (2015), several galaxies with high equivalent width in the [O III] $\lambda 5007$ ($> 3000 \text{ \AA}$ at restframe) lines are studied. They found that those galaxies can be classified as: low-mass, strong starburst, and compact. Following the models of Villaverde et al. (2010), we can assume a maximum equivalent width of the [O II]3727 line for 'normal' galaxies at 150 \AA . Indeed, Kong et al. (2002) found that galaxies with $EW_{[\text{O II}]3727} > 100 \text{ \AA}$ are in the 90th percentile and Thomas et al. (2013), based on data from the SDSS-III/BOSS, showed that galaxies with $EW_{[\text{O II}]3727} > 100 \text{ \AA}$ are located outside the limits of their figures. Being conservative, we can then select for our galaxies a minimum value for high equivalent width galaxies at $\sim 150 \text{ \AA}$.

Based on a first approximation, taking into account the models presented in Villaverde et al. (2010), those high equivalent-width galaxies in [O III] $\lambda 5007$ may be an analogous to our detected emitters with high [O II]3727 equivalent width.

In Table 2, we summarise the properties of the emitters with high [O II]3727 equivalent width. We note we include emitter id:3345, with $EW_{[\text{O II}]3727} = 140 \text{ \AA}$. This is smaller than the selected value of 150 \AA , however, the error in the equivalent width

associated with this emitter makes it compatible with a galaxy with high equivalent width in [O II]3727.

The emission at the line [O II]3727 is influenced by metallicity and the star formation history (see e.g. Anders & Fritze-v. Alvensleben 2003). It was also noted in Villaverde et al. (2010) that $EW_{[\text{O II}]3727}$ presents an important mass and metallicity dependence for ages lower than $\sim 4.5 \text{ Myr}$, and with no dependence at older ages. On the other hand, the $EW_{[\text{O III}]5007}$ has a negligible dependence with the mass. For this reason, a region with large $EW_{[\text{O II}]3727}$ may not simultaneously have a large $EW_{[\text{O III}]5007}$, and they may not be the same type of object. From Table 2, it is clear that the emitters id:3077 and id:8532 have both masses that put them in the low-mass galaxy regime. Moreover, we have complete morphology data for emitter id:8532 and it seems to point out towards a disc-like emission galaxy. This may also indicate also that a high [O III] equivalent-width objects are not the same type of emitters as the ones with high [O II]3727 equivalent width. Unfortunately, we do not have enough information to establish the correct morphology for all our emitters nor their masses. Nevertheless, we are able to establish an upper limit for the masses of id:3345 and id:6445, both of them well inside the low-mass regime. In Fig. 8 we have represented the cutouts for the emitters with high [O II]3727 equivalent width in the composite OTELO band, obtained by adding all the slices of the scan (see Bongiovanni et al. 2019 for an in-depth description).

In Fig. 9, we represent the [O II]3727 equivalent width in \AA versus the logarithm of the derived mass of our emitters. We stacked our data in bins of 0.5 dex and we added data from other authors: (Paulino-Afonso et al. 2020, P-A20) with galaxies $z \sim 0.8$, (Darvish et al. 2015, D15) with $z \sim 0.5$, and Reddy et al. (2018) with $z \sim 1.5$. We also fitted a simple function using least squares to the data in the form of the following equation:

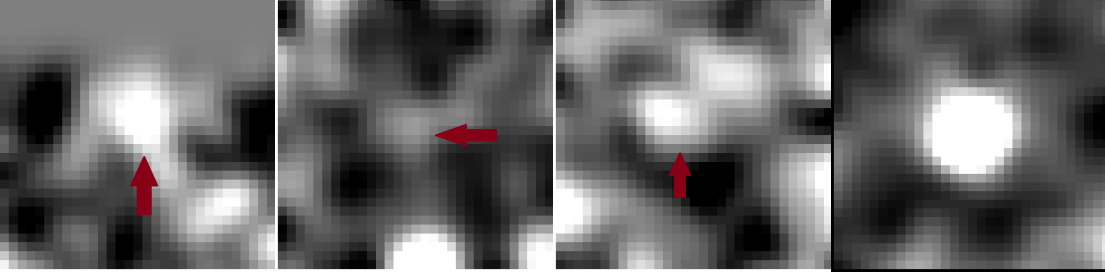
$$EW_{[\text{O II}]3727} = p_1 \times \log(M_*/M_\odot) + p_2. \quad (3)$$

The results of the fitting are given in Table 3 and we also represent the fit obtained from Khostovan et al. (2016) for the [O II]3727, emitters at $z = 1.47$, with its uncertainties, as a pink band. This fit is a power law with the form $EW_{[\text{O II}]3727} = k \times M_*^\beta$, where $\beta = -0.23$ and $\log(k) = 3.79$. As pointed out by Paulino-Afonso et al. (2020), higher stellar mass galaxies have lower equivalent widths in [O II]3727, independently of the environment. They suggest that this trend is mostly a consequence of the underlying main sequence of star-forming galaxies. Our data seems to follow this behaviour. On the other hand, there is a large difference between our data and those of Paulino-Afonso et al. (2020) at higher stellar masses. We must point out that we are sampling lower-mass galaxies than Paulino-Afonso et al. (2020), Darvish et al. (2015), and Reddy et al. (2018). On the other hand, Reddy et al. (2018) seem to have a large value for the equivalent width when compared with other authors (Paulino-Afonso et al. 2020, Darvish et al. 2015), but their results are inside the error margins of ours – and this is not surprising. As Khostovan et al. (2016) have shown, there is also a dependence of the $EW_{[\text{O II}]3727}$ with the redshift, with larger values for $EW_{[\text{O II}]3727}$ when increasing z , up to $z \sim 4$, followed by a decreasing of the equivalent width at higher redshifts. This may be the reason for the lower value of $EW_{[\text{O II}]3727}$ at high stellar masses obtained in Paulino-Afonso et al. (2020), as well as in Darvish et al. (2015), when compared with those presented in Reddy et al. (2018), Khostovan et al. (2016), and this work.

Cava et al. (2015) studied two groups of [O II]3727 emitters: one at $z \sim 0.84$ and other at $z \sim 1.23$. They reached a result a

OTELO ID. #	$EW(\text{\AA})$	C_1	$\log n_I$	$\log N_V^I$	$\log(M_*/[M_\odot])$
3077	153 ± 36	N/A	N/A	N/A	8.17 ± 0.10
3345	140 ± 39	N/A	N/A	N/A	< 7.3
6445	180 ± 46	N/A	N/A	N/A	< 8.6
8532	185 ± 16	2.02	0.3 ± 0.5	0.4 ± 0.6	9.41 ± 0.01

Table 2: Emitters with high [O II]3727 equivalent width

Fig. 8: Thumbnails in the OTELO composite filter (obtained adding all the slices of the scan) for the sources with high equivalent width. The red arrow indicates the location of the source. Each thumbnail has 8×8 arcsec size. From left to right: id:3077, id:3345, id:6445, and id:8532.

Data	p_1	p_2
This work	-20.03	235.5
This work + P-A20 + D15	-23.2	255.8

Table 3: Parameters fitted for the EW –stellar mass relation in Eq.3.

bit below $\log(M_*/M_\odot) < 9$, while for $z \sim 1.23$ and at low mass galaxies, there is little correlation between the equivalent width and the derived stellar mass. This is similar to our results for the non-stacked and stacked sources at low stellar mass. On the other hand, at $z \sim 0.84$, Cava et al. (2015) found a clear correlation between the masses and the equivalent width as that presented in Paulino-Afonso et al. (2020), down to $\log(M_*/M_\odot) \simeq 8.5$. This discrepancy may be due to the low number of sources detected at larger redshifts, so we may assume that the correlation should appear with a set of enough emitters. Nevertheless, our results closely follow the fit from Khostovan et al. (2016) down to $\log(M_*/M_\odot) < 8.5$, even when Khostovan et al. (2016) data has few galaxies below that threshold. Moreover, if we calculate the exponent β for our binned data, we obtain $\beta = -0.20 \pm 0.04$, which agrees, within uncertainties, with the one obtained in Khostovan et al. (2016), $\beta = -0.23 \pm 0.01$.

5. The [O II]3727 luminosity function

Using the data obtained for all the emitters in the catalogue, we derived the LF for the [O II]3727 line emitters at $z \sim 1.43$ after taking into account the main sources for uncertainties and selection effects: the completeness of the sample and the cosmic variance (CV).

5.1. Completeness

To correct for completeness, we have followed the methods described in Bongiovanni et al. (2020). To summarise, several simulations were carried out to calculate the detection probability function from emission-line sources in the OTELO survey. These simulations helped to calibrate the detection probability as a function of the [O II]3727 line flux. This probability function was then fitted by a sigmoid algebraic function (Eq. 4).

$$d = \frac{aF}{\sqrt{c + F^2}}, \quad (4)$$

where d is the fitted mean detection probability, $F = \log(f_{[\text{O II}]3727}) + b$, and $a = 0.961 \pm 0.010$, $b = 18.297 \pm 0.032$, $c = 0.660 \pm 0.099$ are the fitted parameters. In Fig. 10, we show the completeness correction function and the mean detection probability for the emitters at $z \sim 1.43$.

5.2. Cosmic variance

The comoving volume covered by OTELO at the redshift of this catalogue is about $\sim 1.0 \times 10^4 \text{ Mpc}^3$, along with an explored sky area of about 0.015 deg^2 . Because of this small volume (when compared with other surveys; see Table 3), the effects of CV are remarkable. Indeed, Stroe & Sobral 2015 found that volumes smaller than $3 \times 10^4 \text{ Mpc}^3$ are affected in such a way for CV that the results in the determination of the LF could lead to errors up to 100% in the parameters employed to fit the such LF. This is confirmed in Ramón-Pérez et al. (2019), where it was derived a global root of the CV of $\sigma_v \simeq 0.73$, based on the prescription of Somerville et al. (2004), for a comoving volume of $1.4 \times 10^3 \text{ Mpc}^3$ and a redshift of $z \sim 0.40$. And in Bongiovanni et al. (2020), for a mean volume of $6.63 \times 10^3 \text{ Mpc}^3$ and a sample of objects at $z \sim 0.83$, the root CV obtained was $\sigma_{CV} = 0.396$, by using the code³ described in Moster et al.

³ <http://www.usm.uni-muenchen.de/people/moster/home/download.h>

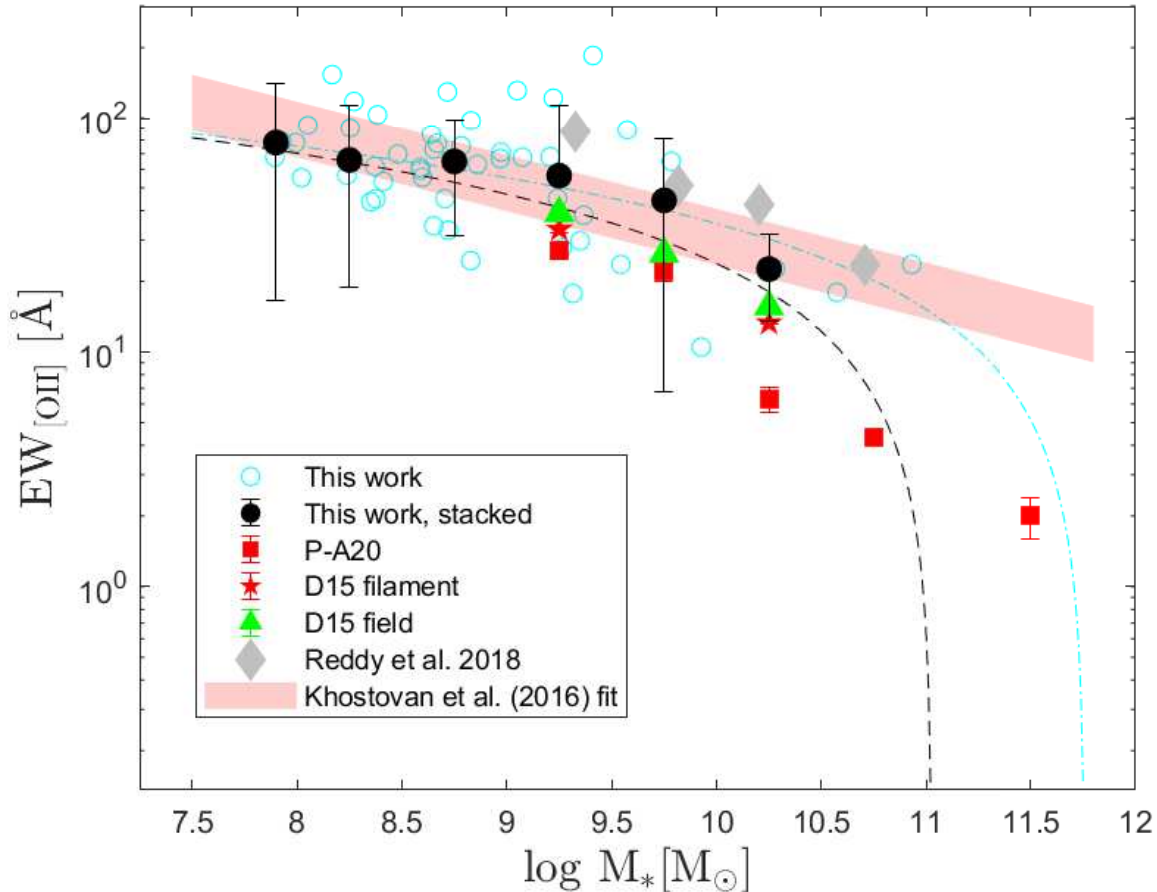


Fig. 9: Relationship between the [O II]3727 equivalent width and the derived stellar mass for our emitters (cyan open circles). The black diamonds are the median of our emitters for bins 0.5 dex in $\log(M_*/M_\odot)$, and the data from Paulino-Afonso et al. (2020) (red closed squares), Darvish et al. (2015) (filled purple stars for filament galaxies and green triangles for field galaxies), and Reddy et al. (2018) (grey diamonds). The black dashed line represents the best fit for all the binned data and the cyan point-dashed line represent the best fit for the only the binned data of the emitters detected in this work. The pink band represents the power law fit with uncertainties from Khostovan et al. (2016) for [O II]3727 emitters at $z = 1.47$.

(2011). It is thus made clear that obtaining an estimation of the CV is a necessary condition if we want to correctly characterise the [O II]3727 luminosity function.

According to the mean number density of [O II]3727 line emitters ($1.4 \times 10^{-3} \text{ Mpc}^{-3}$), it is expected that the CV effects are more pronounced than the estimated for previous OTELO samples at lower redshifts, despite the increased cosmic volume explored at $z \sim 1.43$ as compared to those cases. On this basis, we examined the contribution of the CV to the uncertainty of the LF from each approach used in the OTELO papers referred above. On one side, Somerville et al. (2004) provide a recipe to estimate the CV based on a known average redshift and number density in deep surveys, but unknown clustering strength. The mean root CV obtained for the science case presented here is $\sigma_v \simeq 0.61$. On the other hand, the approach given by Moster et al. (2011) allows us to compute CV as a function of mean redshift, redshift bin size, and the stellar mass of the subject galaxy population. By following this prescription, we were able to estimate an uncertainty function attributed to the CV, $\sigma_{\text{CV}}(M_*)$ for six bins in the stellar mass range $8.5 \leq \log(M_*/M_\odot) \leq 11.5$ for the [O II]3727 sample, and the mean uncertainty obtained for our sample at $\langle z \rangle = 1.43$ is $\langle \sigma_{\text{CV}} \rangle = 0.304$. In view of the noticeable

difference between these estimations, we decided to adopt the Somerville et al. (2004) recipe for being the most conservative one. In the final part of Section 5.3, we further discuss the reliability of this approach for the science case presented in this work.

5.3. [O II]3727 luminosity function

The LF computes the number of galaxies (ϕ) per unit of volume and per unit of luminosity. The Schechter (1976) function is the usual parameterisation method:

$$\phi(L) dL = \phi^* (L/L^*)^\alpha \exp(-L/L^*) d(L/L^*), \quad (5)$$

where L is the luminosity of the emission line ([O II]3727 in our case), ϕ^* is the density number of galaxies, L^* is the characteristic luminosity, and α defines the faint-end slope of the LF.

The value of ϕ was calculated according to Bongiovanni et al. (2020) as follows:

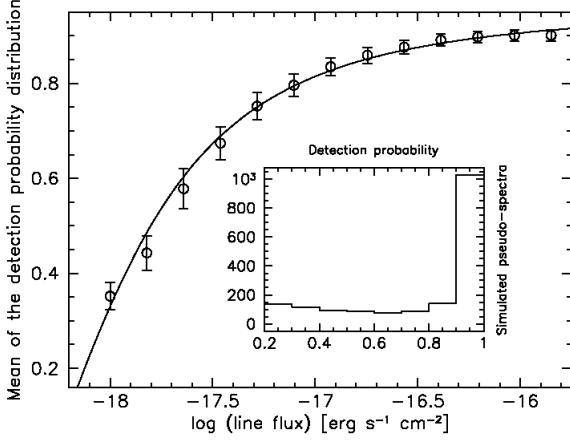


Fig. 10: Mean of the detection probability of the [O II]3727 emitters at $\langle z \rangle \sim 1.43$. As described in Bongiovanni et al. (2020), the inset shows the detection probability distribution obtained from the simulations. The curve represents the least-square weighted fit of the sigmoid function. The bars indicated the mean standard error.

$$\phi[\log L(\text{[O II]3727})] = \frac{4\pi}{\Omega} \Delta[\log L(\text{[O II]3727})]^{-1} \sum_i \frac{1}{V_i d_i}, \quad (6)$$

where d_i is the detection probability for the i th galaxy, obtained with Eq. 4, V_i is the comoving volume for the i th source, Ω is the surveyed solid angle ($\sim 4.7 \times 10^{-6}$ str), and $\Delta[\log L(\text{[O II]3727})] = 0.4$ is the adopted luminosity binning.

The [O II]3727 luminosities based on extinction-corrected line fluxes (Section 3) were sampled in seven bins distributed in the range $40.13 < \log L(\text{[O II]3727}) < 42.93$. For each bin, ϕ values were obtained using Eq. 6. The total uncertainty of each value mainly come from the quadratic combination per luminosity bin of the Poisson error obtained from the number of galaxies, which mean contribution is about 40% (increasing from a 23% for lower luminosity bins up to 70% for the upper-side bin) and the uncertainty associated with the CV. Following the recipe provided by Somerville et al. (2004), the estimated root of the CV, σ_v , increases from 0.6 at the $\log L(\text{[O II]3727}) = 40.33$ bin, to 0.91 at the $\log L(\text{[O II]3727}) = 42.73$ one. Total uncertainty in each bin also includes the contribution of the mean standard error of the completeness correction (5.1) and the probability of incorrect emission-line sources identification (which also includes the fraction of bona fide emitters lost) based on Bongiovanni et al. (2020), amounting together to $\sim 6\%$. The resulting uncertainties from such combinations, along with the LF data are given in Table 4.

In Table 5, we summarise the Schechter parameters derived for the fit of the LF, as well as the parameters for other works at similar redshifts and with the [O II]3727 line (Drake et al. 2013, Ly et al. 2007 and Hayashi et al. 2013). The Schechter model function of Eq. 5 was fitted to the data given in this table using a weighted least-squares minimisation algorithm based on the Levenberg–Marquardt method⁴. Weights are defined as the reciprocal of the squared total uncertainties of LF data.

We used a fixed value for $\log L^*$ obtained as the average of the well-known values from the works presented in Table 5, that

$\log L(\text{[O II]3727})$ [erg s ⁻¹]	$\log \phi$ [Mpc ⁻³ dex ⁻¹]
40.33	-2.54 ± 0.31
40.73	-2.22 ± 0.25
41.13	-2.27 ± 0.27
41.53	-2.55 ± 0.30
41.93	-2.96 ± 0.37
42.33	-3.27 ± 0.46
42.73	-3.57 ± 0.59

Table 4: Binned values of the observed [O II]3727 luminosity function obtained from Equation 6. The computation of the total uncertainties is described in the text.

is, $\log L^* = 42.44$, with a standard deviation of $\sigma = 0.09$. This was done because our sampling over $\log(L^*) \gtrsim 42.5$ is poor, and consequently, $\log L^*$ is completely unconstrained in the fitting process. Assuming this standard deviation as a measure of the $\log L^*$ uncertainty and that it is normally distributed, we estimated the standard errors of the fitted parameters ϕ^* and α from 10^5 realisations of the fitting procedure described above. The uncertainties thus obtained amount 50.3% and 4.2% of the fitted ϕ^* and α values. Due to the limited cosmic volume explored by OTELO, large variances would be expected in the normalisation of the LF after fitting, as confirmed by the error estimate of ϕ^* . The opposite occurs with the uncertainty linked to the faint-end slope of the LF since our sample extends far beyond the lower limits reached by other, similar surveys.

In Fig.11, we represent the LF data for our emitters and their best fittings. The bin with the lowest luminosity ($\log L(\text{[O II]3727}) = 40.33$ [erg/s]) and marked with an open circle, has not been included in the calculations because the method employed to derive the completeness underestimates the number of emitters in the bin, so the errors there are also underestimated. It is clear that our data (represented as black dots) has a lower value for $\log \phi$ at lower luminosities when compared with other works. Consequently, our value of ϕ^* is lower when it is set against those presented in Table 5, and it is a clear effect of the uncertainties on the CV. Nevertheless, as pointed out in Drake et al. (2013), the detection fraction of emitters is very sensitive to the limit of equivalent width in a NB survey, which is of the order of the filter width. So, in this case, as noted in the discussion of Bongiovanni et al. (2020), the lower limit of equivalent width with OTELO survey is about 6 \AA , which is lower than those obtained by the classic narrow-band studies. There, the lower limit for the equivalent width can be over 50 \AA , depending on the technique. This fact comparatively favours the detection of low-mass emitters, despite the CV effects.

It is also worthwhile noting that we sampled the faint end of the LF by almost one dex lower when compared with other authors. We obtained a value for α equals to -1.42 ± 0.06 . This result is similar to that reported by Hayashi et al. (2013), but different from those reported in Drake et al. (2013) and Ly et al. (2007). It must be taken into account that the properties of the sources that serve to create the LFs, such as the luminosity and the extinction, are going to generate different values for α . For example, Sobral et al. (2012) found very different slopes for the

⁴ <https://lmfit.github.io/lmfit-py/index.html>

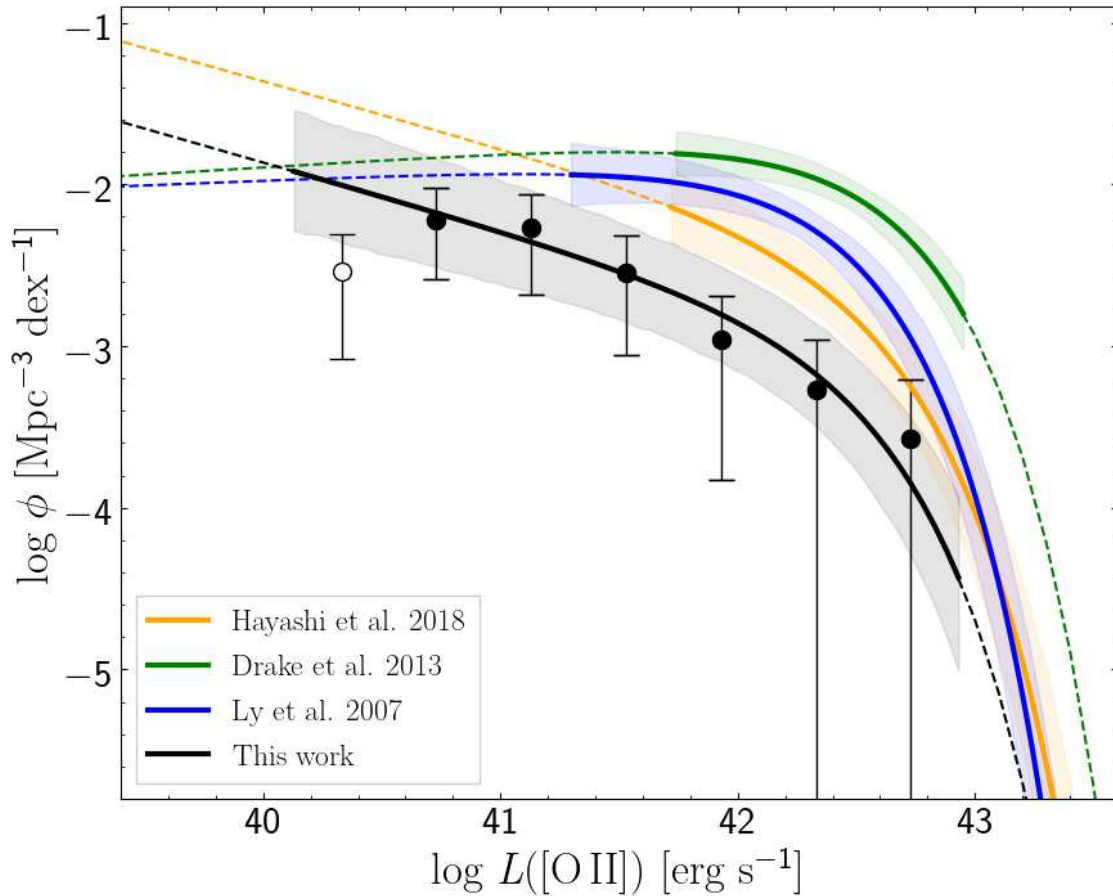


Fig. 11: Luminosity function for the [O II]3727emitters at $z \sim 1.43$ (black circles), with extinction and completeness corrected. The error bars correspond to the total uncertainties given in Table 4, and obtained as described in the text. The open circle marks the lowest luminosity bin and was not employed in the fitting. The black line is the best error-weighted fit of Schechter (1976) function. The green, blue, and orange lines are the LFs from Drake et al. (2013), Ly et al. (2007), and Hayashi et al. (2013) respectively. The shaded areas represent the propagation of 1σ uncertainties of the tabulated LF after 10^4 Monte Carlo realisations. For the OTELO data fitting, this propagation includes the standard deviation of the mean L^* value. In each case, the solid line extend over the sampled luminosity range (see the right side columns in Table 4) and the dashed line is the extrapolation of the corresponding best fit.

LFs for H α and [O II]3727 for galaxies at the same redshift ($z \sim 1.5$) in the HiZELS survey, where $\alpha_{H\alpha} = -1.6 \pm 0.4$ is steeper than $\alpha_{[\text{O II}]3727} = -0.9 \pm 0.2$. Only when calculating the star formation rate (SFR) in an analytical Schechter-like approximation, as Smit et al. (2012) has suggested, the derived α_{SFR} should be similar among studies at the same redshift.

We may explain, in this case, the fair coincidence of our value of α and the one derived in Hayashi et al. (2013), and the difference with Ly et al. (2007) and Drake et al. (2013) following Sobral et al. (2011), where it is suggested that the slope at the faint end of the LF is also affected by the environment. In this case, a steeper slope indicates a low density field. If we made a crude calculation of the density of galaxies presented in the comoving volume, we find that for us it is 5.87 Mpc^{-3} , and for Hayashi et al. (2013), it is even lower, 2.20 Mpc^{-3} . Meanwhile, for Ly et al. (2007) and Drake et al. (2013) is 10.71 Mpc^{-3} and 9.60 Mpc^{-3} , respectively.

Finally, in order to further test the possible contribution of the CV to explain the discrepancies related to the normalisation of the LF, we resampled the OTELO field in 30 i -contiguous cubes containing the 50% of the surveyed cosmic volume and recomputed the LF for each sub-sample (as described above) to obtain $\log \phi_i^*$ and α_i . After that, we calculated the ratio of the standard deviation of the i -parameters and those actually reported in Table 5. The distribution of these ratios are presented in Fig. 12. The median fractional error of ϕ^* and α obtained by this way, 59.9% and 10.7%, respectively, are consistent with the uncertainties associated with these parameters as given in Table 5, despite the volume considered is a half of the explored one. However, taking into account the upper limits of the fractional error distribution of ϕ^* (about 100%), it is clear that the CV could explain the discrepancies observed when our results are compared with those of other surveys that explored much larger cosmic volumes than OTELO, as comprehensively tested by Sobral et al. (2015). But on the other hand, on the basis of this

Source	Method	Number of emitters	$\langle z \rangle$	$\langle V_c \rangle$ 10 ³ Mpc ³	$\log \phi^*$ [Mpc ⁻³ dex ⁻¹]	$\log L^*$ [erg s ⁻¹]	α	$\log L_{min}$ [erg s ⁻¹]	$\log L_{max}$ [erg s ⁻¹]
Ly et al. (2007)	NB	951	1.47	88.48	-2.20±0.06	42.31±0.05	-0.94±0.12	41.30	43.60
Drake et al. (2013)	NB	2218	1.46	230.9	-2.03 ^{+0.04} _{-0.05}	42.52±0.05	-0.91±0.11	41.74	42.95
Hayashi et al. (2013)	NB	11016	1.47	$\sim 5 \times 10^3$	-2.74±0.10	42.48±0.06	-1.41±0.14	41.72	43.48
This work	NB scan	60	1.43	10.21	-3.25±0.21	42.44 (fixed)	-1.42±0.06	40.40	42.50

Table 5: Schechter parameters of the LF([O II]3727) from the recent literature and the best fit of the corresponding OTELO LF, according to data given in Table 4. NB stands for narrow-band. Further details about this fitting are given in the main text.

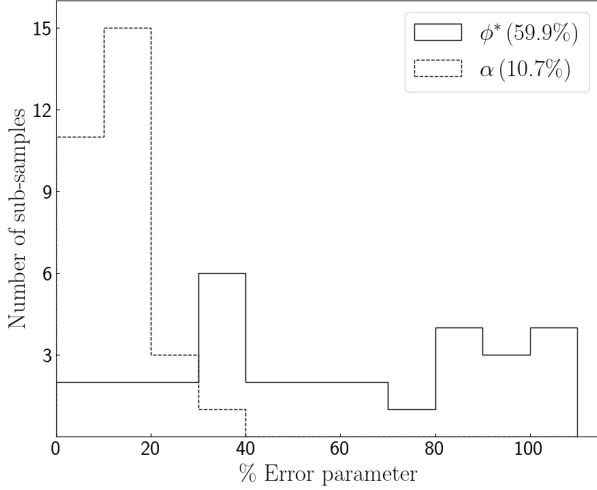


Fig. 12: Fractional error distribution of ϕ^* and α after resampling the the OTELO field in 30 contiguous data cubes and estimate the corresponding luminosity function for testing the cosmic variance effects on these parameters. Values in the upper right corner correspond to the median values of these distributions.

test it is also evident that (i) the theoretical approach adopted in Section 5.2 is enough educated for the purposes of this work; and (ii) the CV effects are less substantial regarding the faint-end slope. This reinforces our appreciation of the sensitivity of OTELO for fairly constraining this parameter.

5.4. Star formation rate density

The LF may be integrated to obtain the total luminosity density. According to Schechter (1976), the integral is equal to:

$$\mathcal{L} = \int_0^\infty \phi(L) L dL = \phi^* L^* \Gamma(\alpha + 2), \quad (7)$$

where Γ is the gamma function.

After the integration, we obtain a value for the total luminosity density of $\log(\mathcal{L}) = 39.38^{+0.16}_{-0.35}$ erg s⁻¹ Mpc⁻³. This luminosity density can be translated to the SFRD via a Kennicutt (1998) equation:

$$\rho(\text{M}_\odot \text{yr}^{-1} \text{Mpc}^{-3}) = (1.4 \pm 0.4) \times 10^{-41} \mathcal{L}[\text{O II}]3727 (\text{erg s}^{-1} \text{Mpc}^{-3}), \quad (8)$$

which is derived employing a Salpeter (1955) initial mass function (IMF). In order to convert this SFRD from the Salpeter

IMF to the Kroupa (2001) IMF, we only need to multiply by a constant factor of 0.67 (Madau & Dickinson 2014). It has to be noted that the direct conversion of [O II]3727 luminosity to SFR may presents several problems, including metallicity and reddening dependencies (Khostovan et al. 2015). Nevertheless, it seems that the reddening is the main factor when deriving the SFR from [O II]3727 lines, as noted in Zhu et al. (2009) and Kewley et al. (2004).

We obtained a final result of $\log(\rho) = -1.65^{+0.28}_{-0.47}$ (erg s⁻¹ Mpc⁻³). In Fig. 13 we plotted our derived value for the SFRD (red filled square) as a function of the redshift. In order to illustrate the SFRD evolution, we complemented the figure with results from the literature. All the data has been converted to a Kroupa IMF. The black dashed line is the fit done by Khostovan et al. (2015) following the parametrisation of Madau & Dickinson (2014):

$$\log(\rho) = a \frac{(1+z)^b}{1 + [(1+z)/c]^d}, \quad (9)$$

where $a = 0.015$, $b = 2.26$, $c = 4.07$, and $d = 8.39$.

It is clear from Fig. 13 that our result is below the curve, in a locus with the [O II]3727 data from the compilation. It must be noted that the SFRDs derived from Khostovan et al. (2015) compilation are not extinction-corrected, unlike our derived value for the SFRD. The data from Khostovan et al. (2015) and Hayashi et al. (2020) are located about ~ 0.25 dex higher. This difference may be attributed to the low value of ϕ^* due to the large uncertainties in the CV, as discussed in Section 5.3. Thereafter, this creates a lower value for the luminosity density when compared with their results, and, consequently, a lower value for the SFRD.

If we integrate our LF, but change the value derived for our ϕ^* by the one obtained in Hayashi et al. (2013), the new derived SFRD (indicated in Fig.13 by the filled red square) is now located over the line defined by Madau & Dickinson (2014) and has almost the same value as the SFRD derived by Khostovan et al. (2015) at the same redshift.

6. Summary and conclusions

We created a catalogue of 60 [O II]3727 emitters at $\langle z \rangle = 1.43$, selected from data of the OTELO survey. We derived, from the pseudo-spectra, the redshifts, fluxes, and equivalent widths of all emitters. In Table A.1, we have catalogued all the emitters of the sample presented in this work. This table will be electronically available at CDS.

Taking advantage of the ancillary data of the OTELO survey, we were able to fit galaxy templates to our emitters through the LePhare code. Thanks to this, we were able to derive extinctions

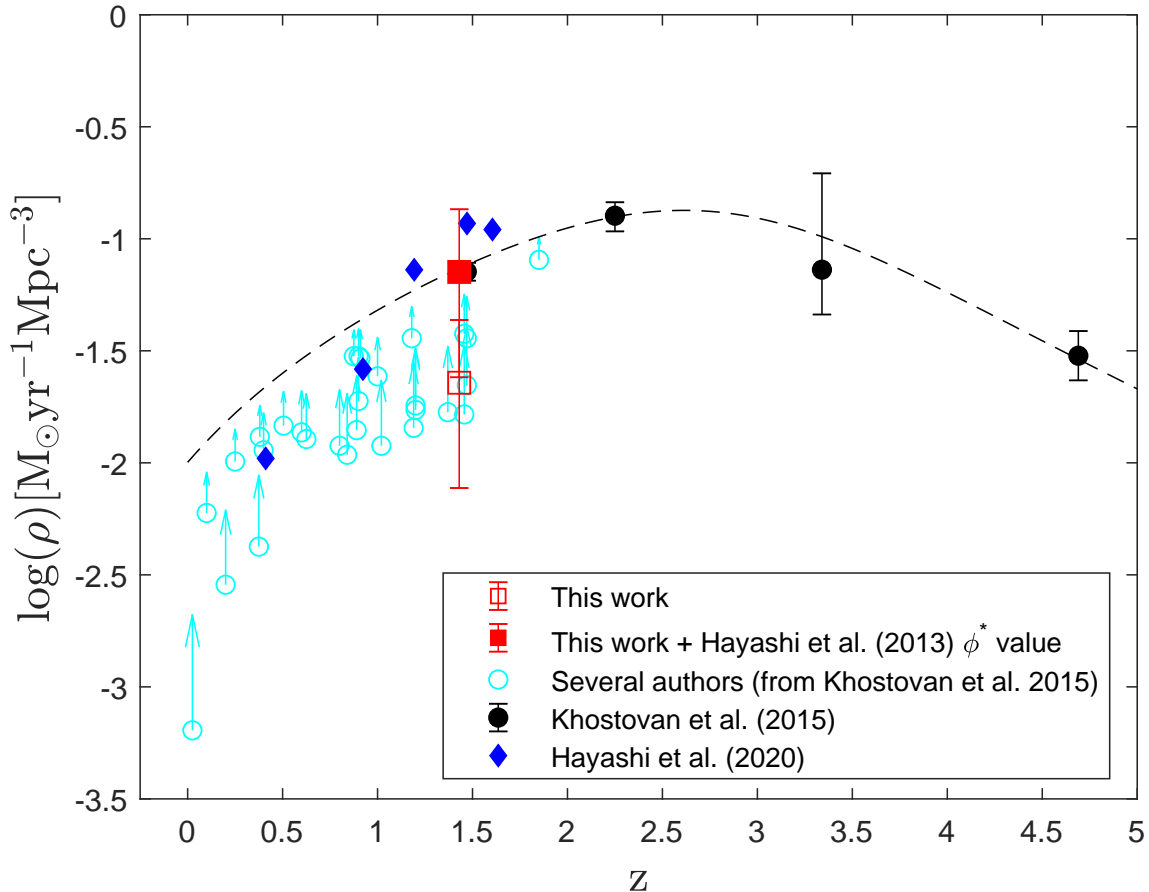


Fig. 13: SFRD evolution for several authors. The cyan circles are SFRD derived from [O II]3727, compiled by Khostovan et al. (2015) in the Table C1 of their paper, and includes data from Ciardullo et al. (2013), Sobral et al. (2012), Bayliss et al. (2012), Ly et al. (2007), Zhu et al. (2009), Takahashi et al. (2007), Glazebrook et al. (2004), Teplitz et al. (2003), Gallego et al. (2002), Hicks et al. (2002), Hogg et al. (1998), and Hammer et al. (1997). We note that these points are not extinction-corrected, so they are a lower limit for the SFRD, as indicated by the cyan arrows. The filled black circles are data from Khostovan et al. (2015). The filled diamonds are data from Hayashi et al. (2020). The result of this work is represented by the open square. The red filled square represents the results of the SFRD from our LF but integrated with the ϕ^* from Hayashi et al. (2013). The black dashed line is the [O II]3727 fit to the Khostovan et al. (2015) data, following the parametrisation of Madau & Dickinson (2014).

for all the emitters and masses (or at least their upper bounds) for all the emitters. In total, 93% of the emitters were low-mass galaxies.

We were also able to obtain morphology parameters (Sérsic and concentration indices) for 44 of the emitters. The sérsic index derived for all of the emitters presented values compatible with disc galaxies. The majority of the [O II]3727 emitters are located in the bluer zone of the $(u - r)$ versus morphology diagrams when compared with the rest of the galaxies of the OTELO survey. Also, all of them were classified as LT using the discriminant developed in de Diego et al. (2020). We detected four emitters with unusually high EW in [O II]3727 (Kong et al. 2002). One of them, id:8532, appears to be a low-mass disc galaxy.

The derived equivalent widths, having been binned and stacked, seem to follow the trends derived in Paulino-Afonso et al. (2020) and Khostovan et al. (2016) with the stellar mass. However, both Paulino-Afonso et al. (2020) ($z \sim 0.8$) and Darvish et al. (2015) ($z \sim 0.5$) present lower values for the equivalent width at larger masses when

compared with Reddy & Steidel (2009), Khostovan et al. (2016) and our data (at $z \sim 1.5$, $z = 1.47$ and $z = 1.43$ respectively). This may be due to the evolution of the equivalent width with the redshift, as suggested in Khostovan et al. (2016). Also, the lack of a clear correlation at lower masses for non-stacked sources detected in our data may be due the scarcity of emitters, as appears to be the case in Cava et al. (2015).

After we applied corrections for the completeness and the cosmic variance, among others, we obtained the LF for the [O II]3727 line, reaching almost 1 dex fainter than the works presented in literature. Nevertheless, our data present a lower value on $\log \phi^*$ when compared with other works. Because of the small cosmic volume sampled by OTELO when compared with modern NB surveys, the cosmic variance effects of the total uncertainties of LF data are quite large, and this propagates to the large variance obtained on this parameter. This effect can explain such differences with data provided in the literature.

On the other hand, the value $\alpha = -1.42 \pm 0.06$ obtained suggests a steeper slope on the faint end of the LF when compared with other authors (Drake et al. 2013 or Ly et al. 2007). This pa-

parameter is much less sensitive to the cosmic variance effects than the normalisation (ϕ^*) of the LF. However, we obtain practically the same result as the one derived in Hayashi et al. (2013). As suggested by Sobral et al. (2011), this low value of α may indicate that we are (as well as Hayashi et al. 2013) sampling a low density field.

We have derived the SFRD by integrating the LF, employing the Kennicutt (1998) relationship and Kroupa (2001) IMF. We have found that the data from Khostovan et al. (2015) and from Hayashi et al. (2020) are at least ~ 0.25 dex higher. This difference seems to come for our low value of ϕ^* when compared with other results from literature (Ly et al. 2007, Drake et al. 2013 or Hayashi et al. 2013) and may be caused by the uncertainties presented in the normalisation of the LF due to CV effects.

The existence of a population of low-mass star-forming galaxies has been confirmed at $z = 1.43$. These galaxies present different characteristics when compared with the more massive populations at the same redshift that have been studied in several other works. This indicates that subsequent surveys with the same scope as demonstrated by OTELO are needed in order to complete a census of the galaxy populations at different epochs of the Universe.

Acknowledgements. This paper is dedicated to the memory of our affable colleague and friend Héctor Castañeda, who passed away on Nov. 19th., 2020. The Authors thank the anonymous referee for her/his feedback and constructive suggestions, which have contributed to significantly improve the manuscript. BC wishes to thank Carlota Leal Álvarez for her support during the development of this paper. JAdD thanks the Instituto de Astrofísica de Canarias (IAC) for its support through the Programa de Excelencia Severo Ochoa and the Gobierno de Canarias for the Programa de Talento Tricontinental grant. This work was supported by the Spanish Ministry of Economy and Competitiveness (MINECO) under the grants AYA2013-46724-P, AYA2014-58861-C3-1-P, AYA2014-58861-C3-2-P, AYA2014-58861-C3-3-P, AYA2016-75808-R, AYA2016-75931-C2-1-P, AYA2016-75931-C2-2-P and MDM-2017-0737 (Unidad de Excelencia María de Maeztu, CAB). This work was supported by the project Evolution of Galaxies, of reference AYA2017-88007-C3-1-P, within the "Programa estatal de fomento de la investigación científica y técnica de excelencia del Plan Estatal de Investigación Científica y Técnica y de Innovación (2013-2016)" of the "Agencia Estatal de Investigación del Ministerio de Ciencia, Innovación y Universidades", and co-financed by the FEDER "Fondo Europeo de Desarrollo Regional". This article is based on observations made with the Gran Telescopio Canarias (GTC) at Roque de los Muchachos Observatory of the Instituto de Astrofísica de Canarias on the island of La Palma. This study makes use of data from AEGIS, a multi-wavelength sky survey conducted with the Chandra, GALEX, Hubble, Keck, CFHT, MMT, Subaru, Palomar, Spitzer, VLA, and other telescopes, and is supported in part by the NSF, NASA, and the STFC. Based on observations obtained with MegaPrime/MegaCam, a joint project of the CFHT and CEA/IRFU, at the Canada-France-Hawaii Telescope (CFHT) which is operated by the National Research Council (NRC) of Canada, the Institut National des Sciences de l'Univers of the Centre National de la Recherche Scientifique (CNRS) of France, and the University of Hawaii. This work is based in part on data products produced at Terapix available at the Canadian Astronomy Data Centre as part of the Canada-France-Hawaii Telescope Legacy Survey, a collaborative project of NRC and CNRS. Based on observations obtained with WIRCam, a joint project of CFHT, Taiwan, Korea, Canada, France, at the Canada-France-Hawaii Telescope (CFHT), which is operated by the National Research Council (NRC) of Canada, the Institut National des Sciences de l'Univers of the Centre National de la Recherche Scientifique of France, and the University of Hawaii. This work is based in part on data products produced at TERAPIX, the WIRDS (WIRCam Deep Survey) consortium, and the Canadian Astronomy Data Centre. This research was supported by a grant from the Agence Nationale de la Recherche ANR-07-BLAN-0228.

References

- Anders, P. & Fritze-v. Alvensleben, U. 2003, A&A, 401, 1063
- Bayliss, K. D., McMahon, R. G., Venemans, B. P., Banerji, M., & Lewis, J. R. 2012, MNRAS, 426, 2178
- Bongiovanni, Á., Ramón-Pérez, M., Pérez García, A. M., et al. 2019, A&A, 631, A9
- Bongiovanni, Á., Ramón-Pérez, M., Pérez García, A. M., et al. 2020, A&A, 635, A35
- Bruzual, G. & Charlot, S. 2003, MNRAS, 344, 1000
- Calzetti, D., Armus, L., Bohlin, R. C., et al. 2000, ApJ, 533, 682
- Cava, A., Pérez-González, P. G., Eliche-Moral, M. C., et al. 2015, ApJ, 812, 155
- Cedr s, B., Beckman, J. E., Bongiovanni,  ., et al. 2013, ApJ, 765, L24
- Ciardullo, R., Gronwall, C., Adams, J. J., et al. 2013, ApJ, 769, 83
- Ciotti, L. 1991, A&A, 249, 99
- Comparat, J., Richard, J., Kneib, J.-P., et al. 2015, A&A, 575, A40
- Darvish, B., Mobasher, B., Sobral, D., et al. 2015, ApJ, 814, 84
- De Barros, S., Oesch, P. A., Labb , I., et al. 2019, MNRAS, 489, 2355
- de Diego, J. A., Nadolny, J., Bongiovanni,  ., et al. 2020, A&A, 638, A134
- Drake, A. B., Simpson, C., Collins, C. A., et al. 2013, MNRAS, 433, 796
- Gallego, J., Garc a-Dab , C. E., Zamorano, J., Arag n-Salamanca, A., & Rego, M. 2002, ApJ, 570, L1
- Garn, T., Sobral, D., Best, P. N., et al. 2010, MNRAS, 402, 2017
- Geach, J. E., Smail, I., Best, P. N., et al. 2008, MNRAS, 388, 1473
- Glazebrook, K., Tober, J., Thomson, S., Bland-Hawthorn, J., & Abraham, R. 2004, AJ, 128, 2652
- Hammer, F., Flores, H., Lilly, S. J., et al. 1997, ApJ, 481, 49
- Harish, S., Coughlin, A., Rhoads, J. E., et al. 2020, ApJ, 892, 30
- Hayashi, M., Ly, C., Shimasaku, K., et al. 2015, PASJ, 67, 80
- Hayashi, M., Shimakawa, R., Tanaka, M., et al. 2020, PASJ[arXiv:2007.07413]
- Hayashi, M., Sobral, D., Best, P. N., Smail, I., & Kodama, T. 2013, MNRAS, 430, 1042
- Herenz, E. C., Wisotzki, L., Saust, R., et al. 2019, A&A, 621, A107
- Hicks, E. K. S., Malkan, M. A., Teplitz, H. I., McCarthy, P. J., & Yan, L. 2002, ApJ, 581, 205
- Hogg, D. W., Cohen, J. G., Blandford, R., & Pahre, M. A. 1998, ApJ, 504, 622
- Huang, X., Zheng, W., Wang, J., et al. 2015, ApJ, 801, 12
- Ibar, E., Sobral, D., Best, P. N., et al. 2013, MNRAS, 434, 3218
- Ilbert, O., Arnouts, S., McCracken, H. J., et al. 2006, A&A, 457, 841
- Kauffmann, G., Heckman, T. M., White, S. D. M., et al. 2003, MNRAS, 341, 54
- Kennicutt, Robert C., J. 1992, ApJ, 388, 310
- Kennicutt, Robert C., J. 1998, ARA&A, 36, 189
- Kewley, L. J., Geller, M. J., & Jansen, R. A. 2004, AJ, 127, 2002
- Khostovan, A. A., Malhotra, S., Rhoads, J. E., et al. 2020, MNRAS, 493, 3966
- Khostovan, A. A., Sobral, D., Mobasher, B., et al. 2015, MNRAS, 452, 3948
- Khostovan, A. A., Sobral, D., Mobasher, B., et al. 2016, MNRAS, 463, 2363
- Kinney, A. L., Calzetti, D., Bohlin, R. C., et al. 1996, ApJ, 467, 38
- Kong, X., Cheng, F. Z., Weiss, A., & Charlot, S. 2002, A&A, 396, 503
- Kroupa, P. 2001, MNRAS, 322, 231
- Lamareille, F., Contini, T., Le Borgne, J. F., et al. 2006, A&A, 448, 893

- Lilly, S. J., Tresse, L., Hammer, F., Crampton, D., & Le Fevre, O. 1995, *ApJ*, 455, 108
- López-Sanjuan, C., Le Fèvre, O., Ilbert, O., et al. 2012, *A&A*, 548, A7
- Ly, C., Malkan, M. A., Kashikawa, N., et al. 2007, *ApJ*, 657, 738
- Madau, P. & Dickinson, M. 2014, *ARA&A*, 52, 415
- Moster, B. P., Somerville, R. S., Newman, J. A., & Rix, H.-W. 2011, *ApJ*, 731, 113
- Nadolny, J., Bongiovanni, Á., Cepa, J., et al. 2021, *arXiv e-prints*, arXiv:2101.06460
- Nadolny, J., Lara-López, M. A., Cerviño, M., et al. 2020, *A&A*, 636, A84
- Navarro Martínez, R., Pérez García, A. M., Pérez-Martínez, R., et al. 2020, in *Contributions to the XIV.0 Scientific Meeting (virtual) of the Spanish Astronomical Society*, 66
- Ouchi, M., Shimasaku, K., Akiyama, M., et al. 2008, *ApJS*, 176, 301
- Park, K., Di Matteo, T., Ho, S., et al. 2015, *MNRAS*, 454, 269
- Paulino-Afonso, A., Sobral, D., Buitrago, F., & Afonso, J. 2017, *MNRAS*, 465, 2717
- Paulino-Afonso, A., Sobral, D., Darvish, B., et al. 2020, *A&A*, 633, A70
- Ramón-Pérez, M., Bongiovanni, Á., Pérez García, A. M., et al. 2019, *A&A*, 631, A10
- Reddy, N. A., Shapley, A. E., Sanders, R. L., et al. 2018, *ApJ*, 869, 92
- Reddy, N. A. & Steidel, C. C. 2009, *ApJ*, 692, 778
- Salpeter, E. E. 1955, *ApJ*, 121, 161
- Schechter, P. 1976, *ApJ*, 203, 297
- Sersic, J. L. 1968, *Atlas de Galaxias Australes*
- Smit, R., Bouwens, R. J., Franx, M., et al. 2012, *ApJ*, 756, 14
- Sobral, D., Best, P. N., Matsuda, Y., et al. 2012, *MNRAS*, 420, 1926
- Sobral, D., Best, P. N., Smail, I., et al. 2011, *MNRAS*, 411, 675
- Sobral, D., Matthee, J., Best, P. N., et al. 2015, *MNRAS*, 451, 2303
- Sobral, D., Santos, S., Matthee, J., et al. 2018, *MNRAS*, 476, 4725
- Sobral, D., Smail, I., Best, P. N., et al. 2013, *MNRAS*, 428, 1128
- Somerville, R. S., Lee, K., Ferguson, H. C., et al. 2004, *ApJ*, 600, L171
- Strateva, I., Ivezić, Ž., Knapp, G. R., et al. 2001, *AJ*, 122, 1861
- Stroe, A. & Sobral, D. 2015, *MNRAS*, 453, 242
- Takahashi, M. I., Shioya, Y., Taniguchi, Y., et al. 2007, *ApJS*, 172, 456
- Teplitz, H. I., Collins, N. R., Gardner, J. P., Hill, R. S., & Rhodes, J. 2003, *ApJ*, 589, 704
- Thomas, D., Steele, O., Maraston, C., et al. 2013, *MNRAS*, 431, 1383
- Vika, M., Vulcani, B., Bamford, S. P., Häußler, B., & Rojas, A. L. 2015, *A&A*, 577, A97
- Villaverde, M., Cerviño, M., & Luridiana, V. 2010, *A&A*, 517, A93
- Zhu, G., Moustakas, J., & Blanton, M. R. 2009, *ApJ*, 701, 86

Appendix A: Catalogue and pseudo-spectra of the [O II]3727 emitters

In Table A.1, we summarise the main properties of our emitters. The distribution of columns is as follows: the first column is the OTELO identification number, the second and third columns are the coordinates of the sources in degrees, the fourth column is the redshift derived from the deconvolved model (z_{OTELO}), the fifth column is the extinction in mag, the sixth column is the extinction corrected flux in units of 10^{-17} erg/cm²/s, the seventh column is the [O II]3727 equivalent width in Å, and the last column is the derived stellar mass. This table will be available electronically on CDS.

In Fig. A.1, we represent, for all the emitters, the pseudo-spectrum flux in erg/cm²/s/Å (black dots and black lines) and the deconvolved model (red line and same units), as a function of the wavelength in Å.

Table A.1: Selected emitters

OTELO ID. #	RA [deg]	DEC [deg]	z_{OTELO}	E(B-V) [mag]	Flux [O II]3727 [10^{-17} erg/cm ² /s]	E.W. [Å]	$\log(M_*/[M_\odot])$
00021	214.46764	52.41016	1.4142±0.0012	0.05	0.48±0.16	93±50	8.05±0.53
00381	214.40169	52.41219	1.4692±0.0004	0.16	0.87±0.23	62±40	8.37±0.10
00409	214.37597	52.41288	1.4287±0.0010	0.05	0.41±0.10	53±18	8.41±0.04
00723	214.40686	52.41580	1.4247±0.0010	0.10	0.62±0.12	71±16	8.97±0.10
00863	214.45145	52.41798	1.4280±0.0010	0.45	7.90±1.60	68±18	9.07±0.05
01039	214.48717	52.41881	1.4178±0.0012	0.05	0.24±0.07	68±29	7.89±0.18
01094	214.31071	52.42011	1.4184±0.0012	0.25	1.80±0.55	97±40	8.83±0.08
01191	214.41452	52.42083	1.4285±0.0012	0.26	1.10±0.33	65±23	N/A
01203	214.48628	52.42192	1.4181±0.0009	0.05	1.70±0.20	130±33	8.72±0.03
01359	214.42263	52.42350	1.4261±0.0016	0.10	0.48±0.35	58±52	N/A
01494	214.45005	52.42484	1.4292±0.0009	0.15	1.20±0.25	61±16	8.59±0.09
01535	214.45148	52.42487	1.4263±0.0011	0.05	0.35±0.10	45±17	8.38±0.11
01777	214.47556	52.42722	1.4277±0.0010	0.00	0.22±0.05	78±30	8.67±0.09
01890	214.43149	52.42841	1.4299±0.0013	0.25	1.10±0.46	85±44	8.64±0.15
01969	214.46984	52.43001	1.4297±0.0010	0.05	0.64±0.15	60±18	8.59±0.04
02090	214.32741	52.43109	1.4253±0.0010	0.00	0.46±0.11	77±23	N/A
02480	214.29067	52.43492	1.4175±0.0010	0.05	0.46±0.18	90±71	8.25±0.19
02814	214.39153	52.43922	1.4353±0.0003	0.20	1.30±0.17	65±15	9.78±0.13
03077	214.45529	52.53075	1.4155±0.0007	0.05	1.10±0.18	150±36	8.17±0.10
03155	214.40408	52.52958	1.4619±0.0004	0.20	4.20±0.62	24±4	10.9±0.01
03345	214.32088	52.52815	1.4060±0.0005	0.05	0.81±0.15	140±39	N/A
03633	214.48850	52.52531	1.4053±0.0012	0.05	0.53±0.22	79±41	7.93±0.51
03669	214.47178	52.52496	1.4123±0.0011	0.74	27.0±6.80	85±35	N/A
03707	214.41281	52.52459	1.4176±0.0020	0.36	1.60±1.30	75±77	N/A
04070	214.36268	52.52005	1.4190±0.0018	0.16	1.20±0.39	73±28	8.65±0.03
04308	214.34333	52.51710	1.4646±0.0008	0.10	3.60±0.62	18±3	10.6±0.01
04313	214.38326	52.51718	1.4283±0.0003	0.16	1.60±0.27	38±7	9.37±0.01
04456	214.39479	52.51559	1.4290±0.0010	0.16	1.10±0.25	55±17	8.02±0.11
04611	214.41167	52.51229	1.4498±0.0008	0.16	3.20±0.45	24±4	9.54±0.01
04814	214.43320	52.51136	1.4458±0.0008	0.16	1.40±0.23	120±29	8.27±0.09
05078	214.34538	52.47537	1.4310±0.0010	0.05	0.24±0.06	78±34	7.99±0.10
05090	214.41584	52.47524	1.4771±0.0003	0.10	1.50±0.14	89±14	9.57±0.03
05260	214.31066	52.47391	1.4258±0.0011	0.30	1.30±0.39	33±14	8.72±0.04
05957	214.30764	52.46609	1.4737±0.0012	0.16	0.88±0.36	28±13	9.26±0.01
06196	214.47412	52.46364	1.4484±0.0009	0.00	0.22±0.08	45±19	9.24±0.06
06398	214.37361	52.46292	1.4580±0.0010	0.16	0.29±0.11	45±20	8.71±0.04
06445	214.47302	52.46081	1.4410±0.0007	0.45	1.40±0.26	180±46	N/A
06758	214.40821	52.45696	1.4439±0.0010	0.00	0.21±0.08	59±28	N/A
06844	214.30997	52.45600	1.4267±0.0013	0.16	0.44±0.13	55±23	N/A
06959	214.46646	52.45496	1.4291±0.0012	0.00	0.19±0.06	63±26	8.86±0.12
07183	214.46175	52.45150	1.4359±0.0011	0.45	3.90±1.70	10±5	9.93±0.01
07431	214.36263	52.44858	1.4601±0.0003	0.05	2.60±0.19	130±13	9.05±0.01
07623	214.30638	52.44692	1.4301±0.0010	0.00	0.42±0.14	50±20	N/A
08276	214.41274	52.44036	1.4414±0.0007	0.30	0.92±0.27	65±29	N/A
08313	214.35177	52.50993	1.4307±0.0012	0.66	17.0±4.50	23±7	10.3±0.01
08333	214.43944	52.51062	1.4264±0.0013	0.16	0.79±0.27	70±36	8.48±0.03
08406	214.41518	52.50931	1.4756±0.0003	0.15	0.63±0.12	67±17	8.97±0.05
08453	214.46035	52.49464	1.4307±0.0012	0.05	0.32±0.10	55±24	8.6±0.04
08532	214.32581	52.50783	1.4255±0.0004	0.16	12.0±0.51	185±16	9.41±0.01
08533	214.33172	52.50768	1.4174±0.0018	0.00	0.25±0.12	44±25	8.35±0.07
09285	214.42861	52.50071	1.4286±0.0013	0.05	0.40±0.13	50±20	N/A
09393	214.34782	52.49960	1.4277±0.0011	0.10	0.80±0.23	68±25	9.21±0.03
09419	214.44289	52.49953	1.4274±0.0011	0.05	0.31±0.10	57±22	8.24±0.09
09532	214.34223	52.49744	1.4606±0.0004	0.16	6.80±0.41	120±14	9.22±0.01
09992	214.41634	52.47749	1.4763±0.0008	0.15	1.70±0.27	30±5	9.35±0.01
10114	214.48834	52.49102	1.4172±0.0013	0.05	0.87±0.20	76±22	8.78±0.02
10272	214.40064	52.48954	1.4742±0.0014	0.16	0.53±0.27	25±15	8.83±0.01
10628	214.36998	52.48522	1.4827±0.0014	0.16	0.40±0.17	34±16	8.65±0.02
10808	214.29183	52.48187	1.4146±0.0013	0.05	0.57±0.16	100±45	8.38±0.24
10814	214.36935	52.48267	1.4306±0.0018	0.15	0.61±0.37	18±11	9.31±0.01

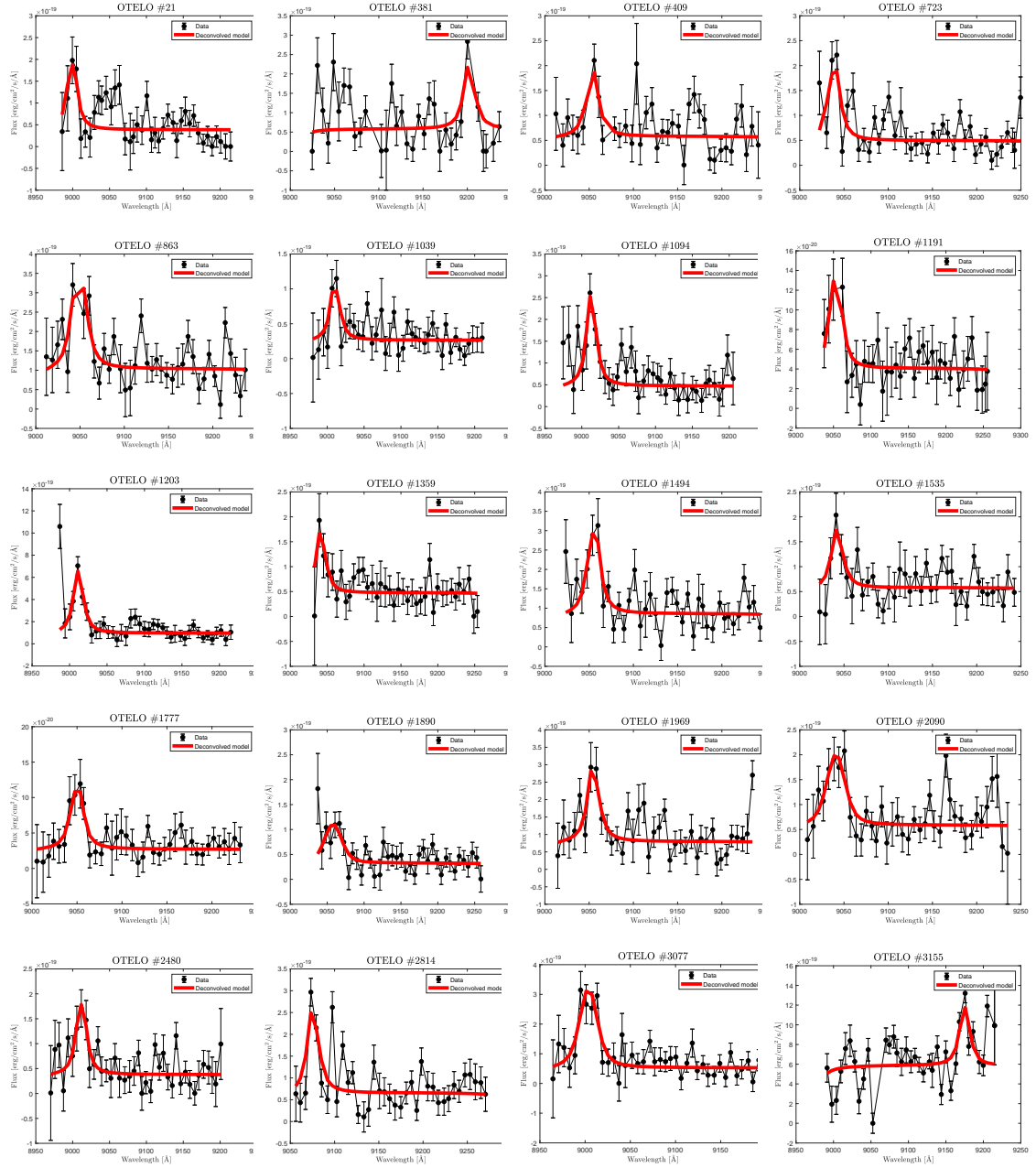


Fig. A.1: Pseudo-spectra of the selected emitters. Black dots represent the measured pseudo-spectra, the red line is the best fitted deconvolved spectra.

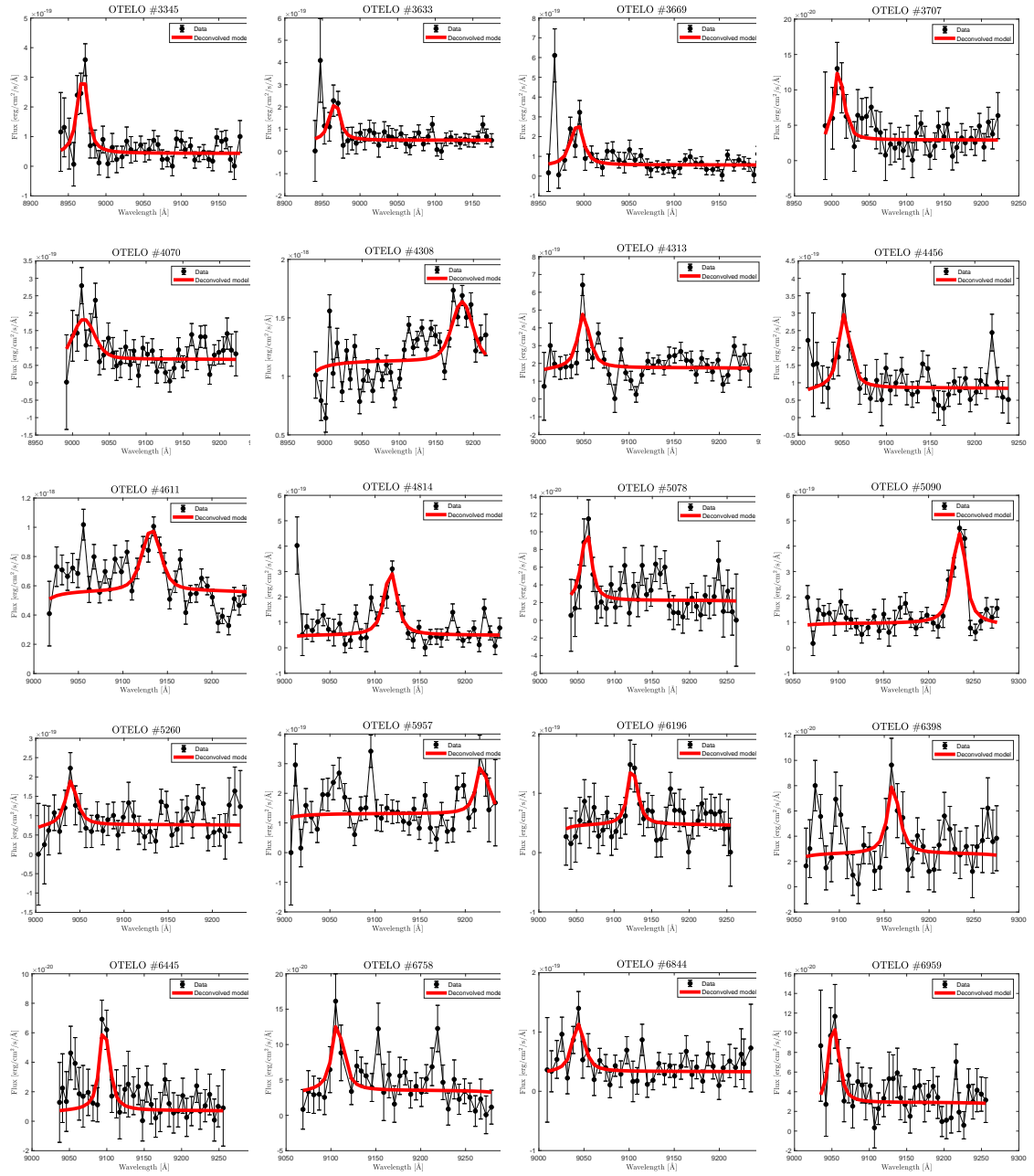


Fig. A.1: Pseudo-spectra of the selected emitters. Black dots represent the measured pseudo-spectra, the red line is the best fitted deconvolved spectra.

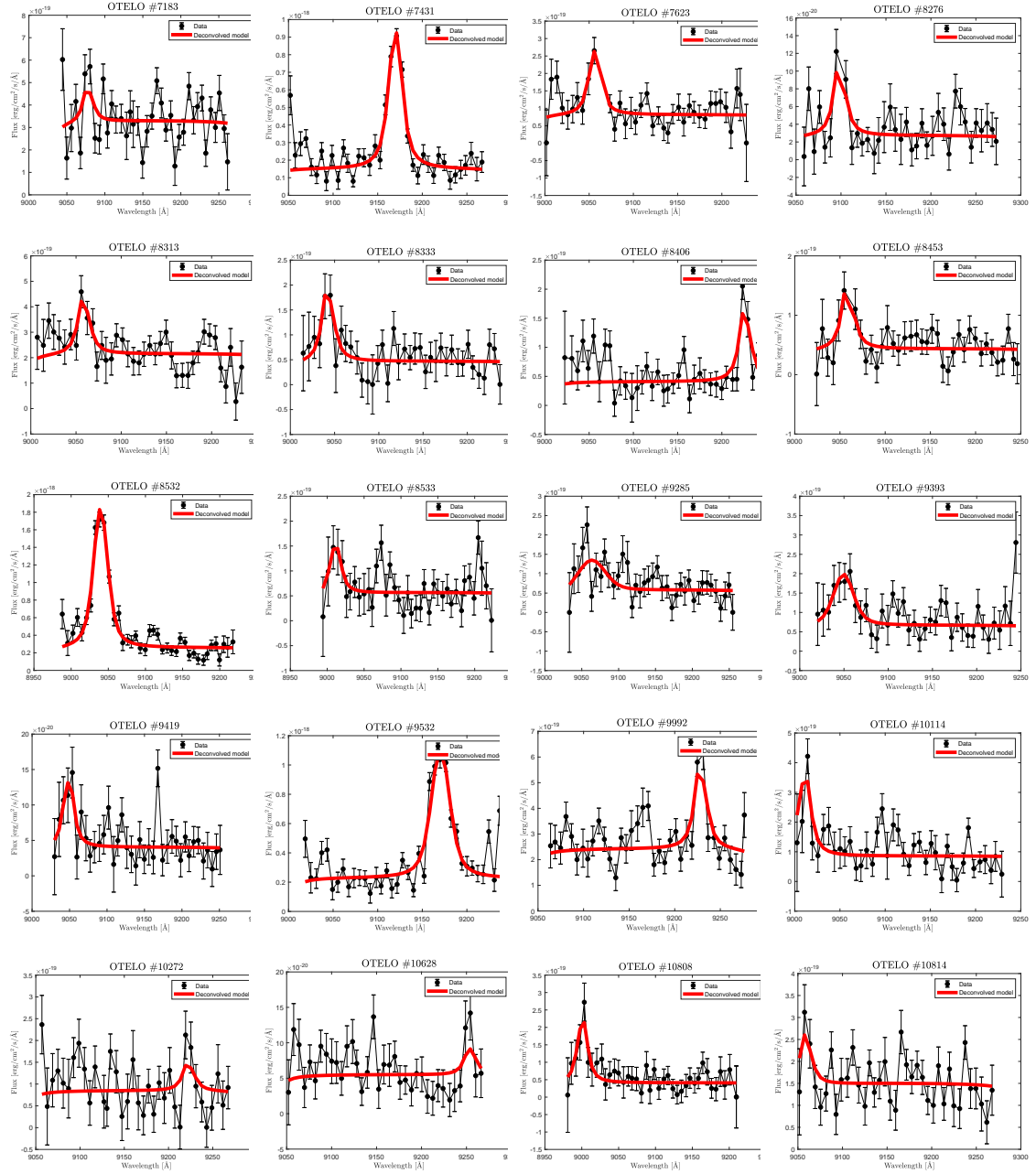


Fig. A.1: Pseudo-spectra of the selected emitters. Black dots represent the measured pseudo-spectra, the red line is the best fitted deconvolved spectra.